Focused Atmospheric-Pressure Microsputterer for Additive Manufacturing of Microelectronics Interconnects

by

Yosef S. Kornbluth

B.A Physics, B.A. Mathematics

Yeshiva University, 2016

SUMBITTED TO THE DEPARTMENT OF MECHANICAL ENGINEERING IN PARTIAL FULFILLMENT OF THE REQUIREMENTS FOR THE DEGREE OF

MASTER OF SCIENCE IN MECHANICAL ENGINEERING

AT THE

MASSACHUSETTS INSTITUTE OF TECHNOLOGY

JUNE 2018

© 2018 Massachusetts Institute of Technology. All rights reserved.

Signature redacted

Signature of Author ______________________

Department of Mechanical Engineering
May 10, 2018

Signature redacted

Certified by ______________________

Luis Fernando Velásquez-García
Principal Research Scientist, Microsystems Technology Laboratories
Thesis Supervisor

Signature redacted

Certified by ______________________

David Hardt
Ralph E. and Eloise F. Cross Professor of Mechanical Engineering
Thesis Reader

Signature redacted

Accepted by ______________________

Rohan Abeyaratne
Chairman, Department Committee on Graduate Theses

Focused Atmospheric-Pressure Microsputterer for Additive Manufacturing of Microelectronics Interconnects

by

Yosef S. Kornbluth

Submitted to The Department of Mechanical Engineering in Partial Fulfillment of the Requirements for the Degree of

Master of Science in Mechanical Engineering

At The

Massachusetts Institute of Technology

Abstract

The past decade has seen a new manufacturing revolution, in the form of additive manufacturing. While recent additive manufacturing processes can produce structural materials in intricate shapes not previously possible, additive manufacturing of functional materials remains a challenge. In particular, functional electronics must still be made via traditional lithographic and etching processes. This thesis introduces a microsputtering method to directly write metals with high resolution. A wire feed enables continuous, extended use of the system. We motivate, simulate, and test a novel electrostatic focusing system to improve the resolution of the imprints; this focusing scheme combines electrostatic and fluid effects to direct the sputtered material into a strip as narrow as 9 μm. The microstructure of the deposits, which affects their conductivity, is also explored and modified. Using gold as printable feedstock, this technology allows for smooth (55 nm roughness) deposits with ~65X the electrical conductivity of bulk metal.

Thesis Supervisor: Luis Fernando Velásquez-García

Title: Principal Research Scientist, Microsystems Technology Laboratories

Acknowledgements

This work was performed in the Microsystems Technology Laboratories, under the supervision of Dr. Luis Fernando Velásquez-García, in collaboration with staff from MIT Lincoln Laboratory. This work was supported in part under Air Force Contract No. FA8721-05-C-0002 and/or FA8702-15-D-0001. Any opinions, findings, conclusions or recommendations expressed here are those of the author and do not necessarily reflect the views of the U.S. Air Force.

I would like to express my appreciation to Dr. Luis Fernando Velásquez-García, for his consistent guidance, particularly in knowing how to help me when I needed it, but giving me the freedom to impart my own mark on the research; to Dr. Lalitha Paramwasaran, for her patience with an inexperienced experimentalist, and hundreds of hours in taking measurements; to Richard Mathews, whose excitement over a new CAD is infectious; to Dr. Livia Racz, for helping ensure that our research is useful and funded; to Professor David Hardt, for guiding me through the subtle requirements of the Mechanical Engineering Department; and to Leslie Reagan, who gives the small-department caring feeling to hundreds of students at a time.

I wouldn't have gotten to graduate school without guidance and support earlier in life; for that, I thank my parents, who taught me that everything worth doing is worth doing well; Dr. Sergey Buldyrev, who introduced me to the thrill of research, and Dr. Edward Berliner, who showed me that sometimes, it's just about "cranking through it" until you change the world.

Thank you Yulia, for supporting me as I worked with "our printer", and understanding my working on Sundays. You are a constant source of encouragement and a pillar to lean on. And to Shevi, whose smile and wave to "Abba Fix-it Man" can turn any day into a great day.

Research is the art of peeling back the unknown, and in that light, I would like to express my gratitude to my Creator, who gave us the opportunity to understand parts of His universe, and by extension, Him. I will close this dedication with the words of Psalms:

השמים מספרים כבוד א-ל ומעשה ידיו מגיד הרקיע

The heavens tell the glory of God, and the sky proclaims His handiwork.

Contents

1 - Introduction 7
2 - Prior Work 8
3 - Theoretical Background 12
3.1- Plasma 12
3.2- Microplasmas 14
3.3- Sputtering 14
3.4- Microplasma Sputtering 15
4 - Experimental Setup 17
4.1- Focusing 17
4.2- Gas Flow 21
4.3- Wire Feed 23
4.4- Substrate 24
5 - Simulation 25
5.1- Model 25
5.2- Results 29
6 - Experimental Results 35
6.1- Composition 35
6.2- Focusing 36
6.3- Roughness 38
6.4- Film microstructure 38
6.5- Deposition Rates 42
7 - Future Work 43
8 - Bibliography 45

List of Tables, Equations, and Figures

Tables

Table I. Alternative printing Methods 11

Table II. Printhead dimensions 22

Equations

Equation 1. Voltage drop between molecular collisions 14

Equation 2. Conservation of mass 18

Equation 3. Conservation of mass- cylindrical 18

Equation 4. Debye length 26

Equation 5. Cost function for optimal focusing 29

Figures

Figure 1. Electrical properties of a typical plasma. 13

Figure 2. Schematic of imprint 19

Figure 3. Schematic of printhead support system 20

Figure 4. Schematic of crosssection of printhead, and support system 21

Figure 5. Physics model. 27

Figure 6. Geometry simulated 28

Figure 7. Deposit shape and yield vs. gap size. 31

Figure 8. Deposit shape and yield vs. focus voltage 32

Figure 9. Plasma plume shape vs. gap size 33

Figure 10. Effects of parameters on focus and yield 34

Figure 11. EDX measurements. 35

Figure 12. Experimental proof of focusing 36

Figure 13. A deposit with a halo. 37

Figure 14. Roughness of deposits 38

Figure 15. Microstructure of deposits 40

Figure 16. Electrical resistance of a deposit. 41

1- Introduction

Modern electronics require complex circuitry, squeezed into as small of a space as possible. State-of-the-art microelectronics manufacturing uses lithography, a method that involves laying down photoresist, tracing out patterns with light, and removing unwanted material via etching. This can achieve in-plane resolution of tens of nanometers with ease, but involves difficult and costly pre- and post-processing. The subtractive nature of traditional lithography also requires the manufacture of expensive masks, limiting the adoption of new circuit designs. The capital expense involved in building the infrastructure necessary for precise deposition and removal of the different layers also acts as a hurdle to inexpensive, agile circuit building.

Thus, lithography can be compared to the state of manufacturing before the additive manufacturing (AM) revolution. Traditional manufacturing is unmatched in its ability to produce high-quality parts in bulk, usually by removing unwanted material from stock. However, over the past decade, AM has demonstrated its utility and versatility in the fast-turnaround development of prototypes, fabrication of customized structures e.g., prosthetics, and in mid-scale production of finished products in a range of materials including polymers and more recently, metals [1],[2]. In addition, AM has made possible the implementation of designs not previously attainable due to fabrication complexity or design three-dimensionality [3],[4].

Similarly, although lithography will likely remain the method of choice for standard chips, there is a need for AM of microelectronics to repair circuits, to produce custom-built chips at a fraction of the cost of a mask, and to manufacture devices on a wider variety, e.g., curved, substrates. Even if the main circuitry is printed using traditional methods, AM can add interconnects on a non-planar surface, allowing the direct interfacing of a variety of devices [5].

In this thesis, a method for AM of metals (and other materials) used in microelectronics and MEMS is explored. The method harnesses a plasma at atmospheric pressure to create high-resolution, high-quality imprints via sputtering without any post-processing, e.g., patterning. Chapter 2 is a review of the literature on AM of metal microstructures, while Chapter 3 explains the theoretical background of plasma microsputterers. Chapter 4 describes the microplasma printer apparatus, while Chapters 5 and 6 report the computational and experimental characterization of the microsputterer, respectively. In Chapter 7, research directions for future work are proposed.

2 - Prior Work

While the technology for AM of plastics is fairly mature, and while there are ways to print structural metals, current methods of printing freeform, finely featured conductive deposits, e.g. interconnects, are all lacking. We outline several of the most promising methods, drawing on the excellent review of Hirt *et al.* [6], and mention their shortcomings. A summary of this exercise is included in Table I.

Arguably, the most mature method for additive manufacturing of freeform, finely featured conductive deposits is nanoparticle ink extrusion, first developed by Lewis in 2003 [7]. Silver nanoparticles are suspended in a liquid (carefully chosen for its rheological properties and ability to be removed during annealing), which is then extruded onto a substrate. Annealing removes the liquid and fuses together the silver, leaving a narrow, conductive line in its wake. Over a decade of research has led to excellent results, with the method eventually becoming commercially available. With high-temperature annealing (250 °C), ~2X the electrical resistivity of bulk silver and in-plane features as small as 2 μm have been achieved [8]. However, annealing limits the substrate choice to materials that can handle such a high temperature. The use of a reactive ink allows for high electrical conductivity with low-temperature annealing, but, due to poor rheological properties, at the expense of minimum feature size [9]. Furthermore, a fundamental limitation of nanoparticle ink extrusion is that is only suitable for silver, which can be properly shaped into nanoparticles that are mixed with solvents to form ink formulations of high concentration without nanoparticle coalescence.

A similar method is electrohydrodynamic printing, or e-jet printing. As in nanoparticle ink extrusion, metallic nanoparticles are suspended in a liquid. By charging the liquid and the substrate, electrostatic fields force nanodroplets out of a small nozzle and onto the substrate. In electrohydrodynamic printing, electrostatic fields deform the meniscus of the liquid into a cone, called the Taylor cone, which emits a jet of liquid from its apex that is chopped into droplets via a Rayleigh instability. The volatile liquid evaporates, leaving behind the dissolved solids, i.e., metallic structures. While submicron features are possible, the voids left by the evaporating ink preclude the formation of conductive structures without further thermal annealing. Even with annealing, the minimum electrical resistivity of the imprints is high, i.e. ~130X that of the bulk

metal [10].

Another commercially available method is laser-induced forward transfer (LIFT). A transparent substrate is coated with a very thin layer of metal. A highly focused laser is aimed at the non-metallic side of the substrate; the applied heat melts a small amount of metal, which flies from the donor substrate to a second substrate, less than a millimeter away, where it is deposited. However, because this method deposits metal in a droplet-by-droplet fashion, electrical conductivity is less than ideal (electrical resistivity is ~12X that of the bulk metal). Additionally, the transparent substrates are not simple to produce, and are depleted quickly; even sparse patterns, where a small fraction of the donor substrate is used, render the donor substrate unsuitable for future use. In addition, because the inter-substrate gap is so small, this method is not suitable, in general, for curved surfaces [11].

Other methods of AM of electronics-quality metal are electron beam induced deposition and ion-beam induced deposition, in which a highly-focused beam of charged particles reacts with a precursor to precipitate a metal deposit. While the feature resolution is excellent [12], the precursor's remnants cause unacceptably high electrical resistance. Although there are a number of chemical post-processing [13] and thermal annealing [14] methods that ameliorate the electrical resistance issue, they can damage the substrate and still result in an unacceptably high resistance.

Similarly, laser assisted electrophoretic deposition precipitates nanoparticles out of a precursor [15]. However, it does so with electrophoresis, in which a carefully focused laser (or other electric field) selectively moves metallic nanoparticles toward a focused spot. There, with the aid of another electric field, the nanoparticles adhere to a charged substrate. To the best of our knowledge, the electrical resistivity of deposits created via this method has not yet been reported in the open literature, but, as with all other methods that combine nanoparticles, the electrical conductivity is most likely significantly less than that of bulk metal; additionally, micrographs of the imprints suggest that they should have high electrical resistivity.

Instead of attempting to manufacture metal components *in situ*, perhaps one of the simplest and more effective methods is to embed already-drawn wires made of bulk metal into a printed plastic structure [16]. While the electrical conductivity is unmatched, the feature size is limited to the size of the wire, approximately 100 μm. Additionally, the printing procedure only allows the

metallic components to be deposited in series with the plastic, instead of at the same time. Thus, metal can only be deposited in the plane of the plastic, not through several layers of printed plastic.

Other researchers have attempted to use established 3D printing technology for plastics to attain finely featured structures with high electrical conductivity. In a mainstream commercial 3D printing system known as fused filament fabrication (FFF) or fused deposition modeling (FDM), thermoplastics are heated until they are soft and then extruded through a nozzle; it is possible to dope the plastic with micro and nanoparticles to attain electrical conductivity, albeit far less than bulk. The resolution is also not high; the minimum feature size is ~150 μm. However, this method is uniquely suitable for printing large conductive structures. [17].

Alternatively, the metal itself can be heated and extruded. Solder alloys soften at significantly lower temperatures than those involved in annealing of AM imprints of metal (58 °C vs. 250 °C), and can thus be similarly extruded, and subsequently harden into arbitrary shapes [18],[19]. However, the resolution of the technique is limited by the rheology of the solder and is insufficiently fine for microelectronics.

There are yet other AM methods for metal deposition that rely on the established method of electroplating, which is commonly used to deposit a thin layer of high-quality metal on a free-form conductive surface. This is done by submerging a conductive surface in a liquid solution; an electric potential forces metal to precipitate out of the solution and adhere to the surface. To achieve small feature size, the liquid can be confined [20],[21], or the metal can be confined in salt form while the liquid is unconfined [20]. With this method, submicron resolution is possible, and, as is typical of electroplating, the material quality is high. However, electroplating is only possible with conductive or semi-conductive substrates and a few conductive materials, limiting the utility of this method in the printing of microcircuits.

In this thesis, we investigate sputtering, which, like electroplating, is commonly used to coat large surfaces with a thin layer of high-quality material. However, unlike electroplating, sputtering is suitable for any substrate and nearly any feedstock, including, crucially, semiconductors and dielectrics. We outline the theory behind sputtering and microsputtering in Chapter 3.

Name	Description	Minimum Feature Size	Electrical Resistivity	Shortcomings
Ink extrusion	Silver nanoparticles suspended in a liquid that is extruded and cured	2 μm [8]	2X bulk [8]	Annealing temperature, minimum feature size, choice of material
E-jet printing	Metal nanoparticles suspended in a liquid; EM fields create and guide droplets	500 nm [10]	130X bulk [10]	Annealing temperature, electrical resistivity
LIFT	Laser melts metal particles from donor to substrate	3 μm [11]	12X bulk [11]	Electrical resistivity
EBID/IBID	Electron/ion beam selectively cures precursor	3 nm [12]	220X bulk [13]	Electrical resistivity
Electrophoretic deposition	Laser guides nanoparticles suspended in a liquid	500 nm [15]	N/A	Electrical resistivity (presumed)
Wire embedding	Bulk-extruded wire is fed onto printed surface	100 μm [16]	Bulk [16]	Minimum feature size
Doped Plastics	Metal nanoparticles are added to plastic feedstock, which is extruded	150 μm [17]	5×10^6X Bulk [17]	Electrical resistivity, Minimum feature size
Solder alloys	Alloys heated and extruded, then cooled	800 μm 46[19]	Bulk [19]	Minimum feature size
Electroplating	Metal confined, then transferred to substrate via electroplating	400 nm [20],[22]	8X bulk [21]	Electrically conductive substrates only

Table I: A summary of reported direct-write additive manufacturing methods that produce finely featured, conductive metal microstructures. While each of these methods has advantages, none is free of shortcomings. Additionally, all of these methods only work on metals; the printing of nanoelectronics requires a combination of metals, semiconductors, and dielectrics.

3 - Theoretical Background

3.1 - Plasma

Plasma is the fourth state of matter, in which electrons and ionized species are significant constitutive parts of a gas, to the degree that electromagnetic forces strongly affect the plasma's behavior. A non-thermal plasma is generally maintained by a voltage gradient; this allows already-present electrons to accelerate, gaining the energy necessary to ionize more atoms into ions and electrons upon impact. The electric field also causes separation of charges, which in turn decreases the voltage gradient. If there are multiple gradients that can maintain a plasma, this shielding will cause the plasma to form along the steepest gradient, thus shielding the regions that contain the other gradients.

Broadly speaking, there are three significant regimes of plasma discharge. First, if the voltage gradient (neglecting space charge) is insufficient for electrons to ionize atoms, a *Townsend discharge* is formed; the ionization "chain reaction" does not grow exponentially, and any ionization (due to, for example, cosmic rays) is not self-sustaining [23][23].

Second, if the voltage gradient is large enough to cause electrons to ionize atoms, a self-sustaining reaction occurs, known as a *glow discharge*. Electrons ionize atoms, and as ions migrate toward the cathode, they shield the majority of the plasma from the low voltage of the cathode. Quickly, an equilibrium is reached, and the shielded portion of the plasma (which is split into several regions, including the Faraday dark space and the positive column) sustains a small voltage gradient, with only enough ionization to replenish charged particles lost to recombination. The electrons, which move much faster than the ions, are attracted to the anode, leaving the positive column with a small positive net charge. Closer to the cathode, in the unshielded region, the ions bombard the cathode, releasing electrons; these electrons can ionize atoms due to the high voltage gradient in this "cathode fall", or "cathode glow" [23]. A diagram of the electric field in a glow discharge is presented in Figure 1.

Once the current of the glow discharge is large enough, thermal effects become significant, causing the plasma to evolve into a third regime. A heated cathode is an excellent source of electrons, which ionize atoms near the cathode. The ions are then drawn to the cathode, which

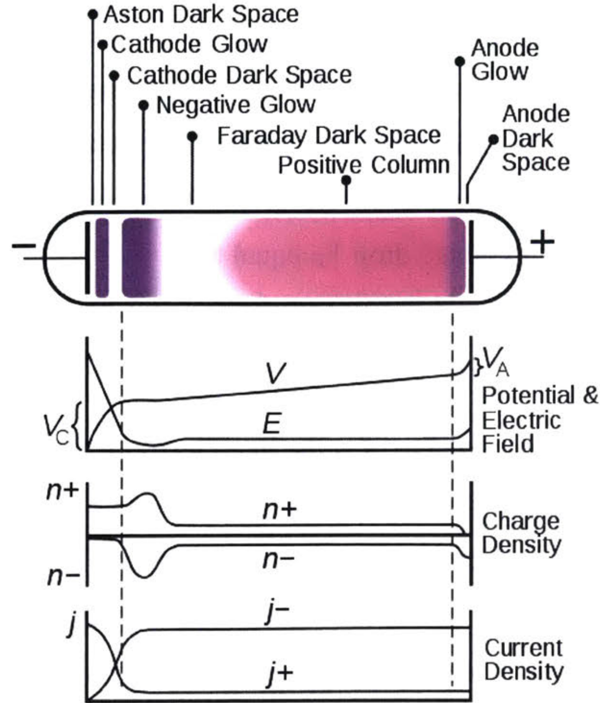

Figure 1. Schematic of the electrical properties potential *V*, electrical field *E*, space charge *n*, and current density *j* of a typical plasma (from [25]). In microplasmas, the only regions of appreciable size are the cathode glow, the Faraday dark space, the positive column, and the anode glow. In our microplasma, the transport of the sputtered material only passes through the cathode glow and Faraday dark space. Note that the electric field is positive (toward the cathode) for the entire plasma, but is strongest in the cathode glow, near the cathode.

heats it further, causing a "runaway" reaction. This is known as *arcing*, due to the formation of an arc –a high-current stream of plasma along the voltage gradient. Arcs often damage the cathode; in the case of a small cathode such as ours, the cathode melts within a few seconds, thus destroying the plasma. Stability is usually achieved through the use of a ballast resistor or other means of current control since arcs are inherently unstable. Several microplasma configurations have been designed to avoid the need for a ballast resistor; we simply use a current-controlled power supply [24].

3.2- Microplasmas

Shortly after plasma research began, Paschen discovered a scaling law described by his eponymous curve [26]. Several behaviors of plasmas are governed by the product of the pressure and the interelectrode distance [23],[27]. On a molecular level, this can be understood by examining the behavior of a single ion. In the distance it travels between collisions with two other particles, the ion will undergo a voltage drop V_D equal to

$$V_D = \frac{V \cdot d}{\lambda}, \tag{1}$$

where V is the interelectrode bias voltage, d is the interelectrode distance, and λ is the mean-free-path of the ion. Given that in an ideal gas the mean-free-path is inversely proportional to the pressure, the product of the interelectrode distance and pressure is an important term. For example, the product of the pressure and the interelectrode distance is relevant in gauging the stability of plasmas; plasmas tend to form at reasonable voltages (1 kV or less) and are well behaved when this product is near 1 Torr-cm [24], which is usually accomplished with the use of a strong vacuum. However, in microplasmas a small interelectrode distance (usually on the order of a millimeter or less) is used instead, allowing for reasonable values of this product –even at atmospheric pressure [24].

Microplasmas have been used in a wide range of applications including mass spectroscopy [29], medical sterilization [30], processing of heat-sensitive polymers [31], excimer sources [32], and nanoparticle synthesis [33], among other reasons, because of their compatibility with atmospheric pressure operation. For our purpose, the printing of fine features and the small scale of the plasma is also advantageous. Additionally, agile manufacturing, our goal, is easier if we obviate the need for a vacuum; sputtering vacuums are typically on the order of 10^{-3} Torr.

3.3- Sputtering

Sputtering is a physical deposition process in which a plasma is used to generate a shower of individual atoms ejected from a target to land on a substrate, producing a conformal coating. A sputterer has two electrodes: a *target* electrode (comprising the material to be deposited), and an

anode electrode. The target is biased at a lower voltage than the anode, causing a plasma to be struck between the electrodes. The electric field between the electrodes accelerates ions toward the target; if a given ion has sufficient energy [28],[34]-[35], it strikes the target with enough force to eject an atom approximately normal to the target surface, with a fraction (~1 eV) of the incident ion's energy. The stream of sputtered atoms moves away from the target to the anode and impinges on a substrate placed at some distance from the target forming a solid deposit, or film. The atom-by-atom creation of the deposit results in a continuous, conformal film; if the sputtered material is a metal, under the right circumstances, this film has high electrical conductivity –approaching that of bulk material.

Sputtering is a well-established technique in the microelectronics industry, where plasmas are struck in large high-vacuum chambers. Thin, flat semiconductor substrates are coated with ultrathin, uniform conductive films, which are then patterned via lithography to form interconnects. Because the material is deposited atomically, many of the defects inherent in the already-described AM techniques can be avoided. Unlike most of the previously described technical approaches, sputtering can be used to create deposits made of most non-crystalline materials, although alloys require special care due to the differences in depletion rates of the different elements that make up the target material [36].

3.4- Microplasma Sputtering

Combining the material quality of sputtering with the atmospheric pressure operation and small dimensions of microplasmas, microplasma sputtering is a promising approach for AM of interconnects; the method harnesses the same physical deposition process used in state-of-the-art microelectronics to manufacture interconnect material, although it operates at a different length scale to directly deposit features without lithographic patterning or the involvement of a high-vacuum environment.

Interest in this technology has sparked two previous explorations into microsputtering. First, Burwell explored a gold target surrounded by a ring anode [37]. Argon was flowed through the gap between the two electrodes, while a magnetic field was used to force precession of the arc formed to limit its harmful effects. Deposits on glass substrates showed excellent electrical

conductivity, although this result may have been due to unintentional thermal annealing (the recorded temperature on the substrate was in excess of 600 °C). The paucity of parameter variation or theoretical modeling is compensated by the innovative experimental setup, which served as an inspiration for our own setup, and by the carefully gathered experimental data.

Second, Abdul *et al.* used a different geometry, in which a plasma is struck directly between a target and a conductive substrate; with this approach, the authors demonstrated the sputtering of copper conductive lines and the completion of a simple thermocouple [38],[39]. Their work includes some helpful measurements of the dimensions of the deposits and the deposition rate. However, their experimental setup is not useful for insulating substrates. Although there is no study of the morphology of the imprints, this investigation confirms an intuitive limitation: the dimensions of the deposit cannot be smaller than the electrode's dimensions. While this limitation can be mitigated by micromachining a target to the desired size of the feature, this is impractical for a consumable target to be used in continuous manufacturing. Our solution to overcome this significant limitation will be discussed in Chapter 4.

4-Experimental Setup

4.1- Focusing

This thesis is motivated in great part by the pressing need to reach higher feature resolution in electrically conductive AM imprints. Just as macroscopically, the size of a graphite impression is governed by the size of a pencil lead, microscopically, the size of a sputter deposit is governed by the size of the target. In our case, machining a sputtering target for continuous deposition down to the necessary resolution for state-of-the-art interconnects (1 μm) would be impractical and potentially unfeasible. Instead, we implement a focusing mechanism.

We thus must focus sputtered gold atoms. Much research into deuterium-tritium fusion has yielded the conclusion that herding neutral atoms is incredibly difficult [40], and the sputtered material in a sputtering plasma is mostly un-ionized [28]. However, there is enough ionized material in the plasma (both sputtered material and working gas) that, if the ions could be directed and the resulting momentum could be transferred to the neutral atoms, the neutrals' movement could be controlled. While the majority of this ionized material is in the cathode fall, we introduce a fast gas flow into the cathode fall region to carry a small fraction of ionized material, far away from the cathode fall, toward the substrate. We harness the dense atmosphere of microplasmas to transfer momentum. While the gases in regular sputterers have very long mean free paths, an ideal gas at atmospheric conditions has a submicron mean free path. The frequency of collisions means that any force on the ions will very quickly transfer to a net change in momentum on the entire plasma, neutrals included.

Therefore, the problem at hand (i.e., the control of neutral atoms), has just been converted to a much simpler and well-studied problem (i.e., the control of ions). Research into charged particle optics (CPO) has yielded several methods to focus ions and electrons onto a single point. This is useful for electron microscopy, as well as several more exotic applications, such as ion microscopy and e-beam lithography. However, the established optical lenses, such as Einzel lens, are not appropriate solutions for our problem. Unlike CPO, our work must take place in atmospheric pressure, and must act on the entire plasma equally. Thus, if we were to try to focus our plasma onto a single spot on a substrate, the pressure differential that this would cause would

negate our efforts. This can be seen by examining the mass flow at any focused spot. Mass must flow in to form the deposit. The sputtered material can adhere to the substrate, but the gas has nowhere to go. Mathematically, the impossibility of single-point focusing in this approach can be derived from the steady-state conservation of mass equation

$$\nabla \cdot (\rho \vec{u}\,) = \rho \nabla \cdot \vec{u} + \vec{u} \cdot \nabla \rho = 0 \tag{2}$$

In cylindrical coordinates with rotational symmetry, equation (2) is equivalent to

$$\rho \left[\frac{\partial u_r}{\partial r} + \frac{u_r}{r} + \frac{\partial u_z}{\partial z} \right] = -u_r \frac{\partial \rho}{\partial r} - u_z \frac{\partial \rho}{\partial z} \tag{3}$$

where u is the velocity of the charged particles, z is the distance from the target to the substrate and r is the radial direction. For the left-hand side of equation (3) to be finite, u_r needs to vanish at $r = 0$; in addition, of a solid surface that does not adsorb gas requires the boundary condition of $u_z = 0$ at the substrate. (Note that this step of the argument is not applicable to traditional CPO). Consequently, the right-hand side of equation (3) must equal 0 at the substrate. However, for beam focusing to be viable, u_r must be negative for small r, and u_z must be positive near the substrate, for the gas to carry the sputtered material to its surface. Therefore, the LHS in equation (3) must be negative, leading to a contradiction. The proposed ion-drag focusing scheme can bypass this limitation by focusing the stream of particles into a narrow line instead of a point –there is no pressure build-up when the gas is constrained in only one dimension. Beam line focusing is achieved by using two pairs of electrodes that are spread evenly around the circumference, and where opposite electrodes are biased at the same voltage (Fig. 2): the plasma is pushed away from the anode electrodes, while the focus electrodes pull the plasma toward them (in fact, defocusing the plasma in that direction), shaping the beam into a line. A benefit of this focused beam profile is that it produces long and narrow lines required for interconnects. The plasma is struck between the anodes and target wire, or, more often, between one of the anodes and the target wire; even though the focus electrodes play no role in the formation of the plasma, they are essential to shape the plasma and focus the imprint.

Ion drag has been used effectively in ion pumps, which are devices that use electric fields to pull ions toward electrode meshes, causing a drag that evacuates neutral gas from a closed vessel

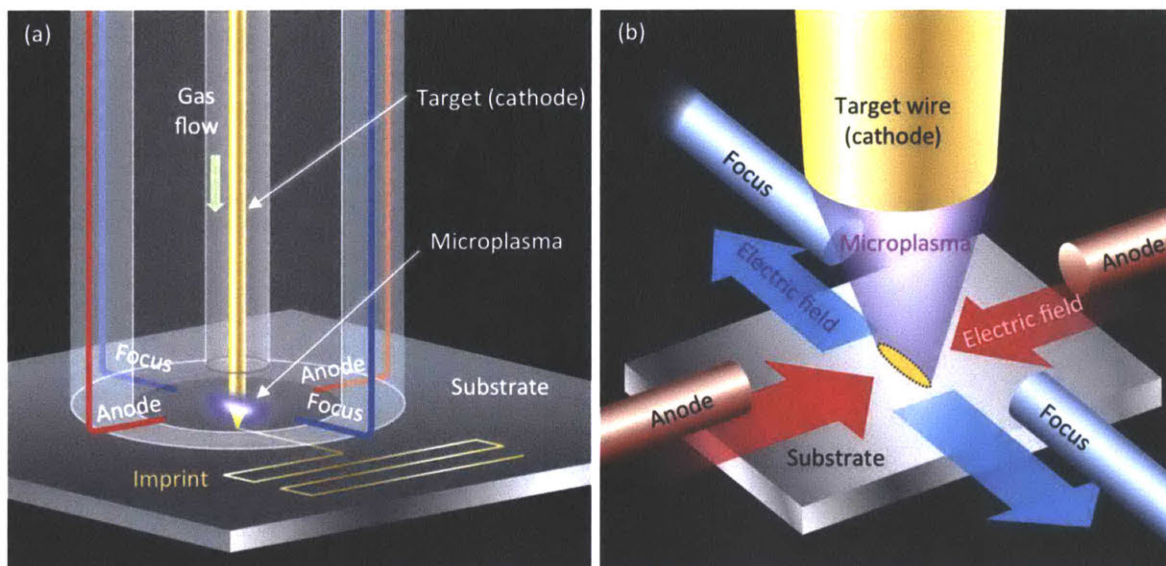

Figure 2. (a) Schematic of the printhead as a metal line is being deposited; (b) close-up schematic of printhead tip showing focused asymmetric imprint spot.

[41]-[43]. Ion drag also has applications in electric-field assisted combustion, where electric fields can shape ion-rich flames, guiding them to where they will best consume fuel [44]-[45]. However, to the best of our knowledge, ours is the first application of ion drag in which the ions are not simply pulled out of the system to the electrodes; we must leave the path to the substrate clear of electrons. We also cannot place a small, negatively charged electrode under the substrate to act as a lodestone. While this might work well for thin, dielectric substrates, conductive substrates would shield the plasma from the attractive effect. Additionally, the effect would not be precise enough if the substrate is too thick (i.e., not on the same order of magnitude as the desired feature size).

We implement the anode/focus electrode system using tungsten wires; tungsten was chosen due to its resistance to sputtering [34],[46], which can affect the electrodes if an undesired plasma forms between the anodes and focus electrodes. The possibility of such sputtering has also been decreased by shortening the focus electrodes; the plasma will tend to follow the sharpest voltage differential, and the target-anode path is much shorter than the anode-focus electrode path, leading to a greater voltage differential. The placement of the electrodes in the printhead can be seen in Fig. 3 (e) and Fig. 4 (a), while an image of a plasma forming between the two anode electrodes

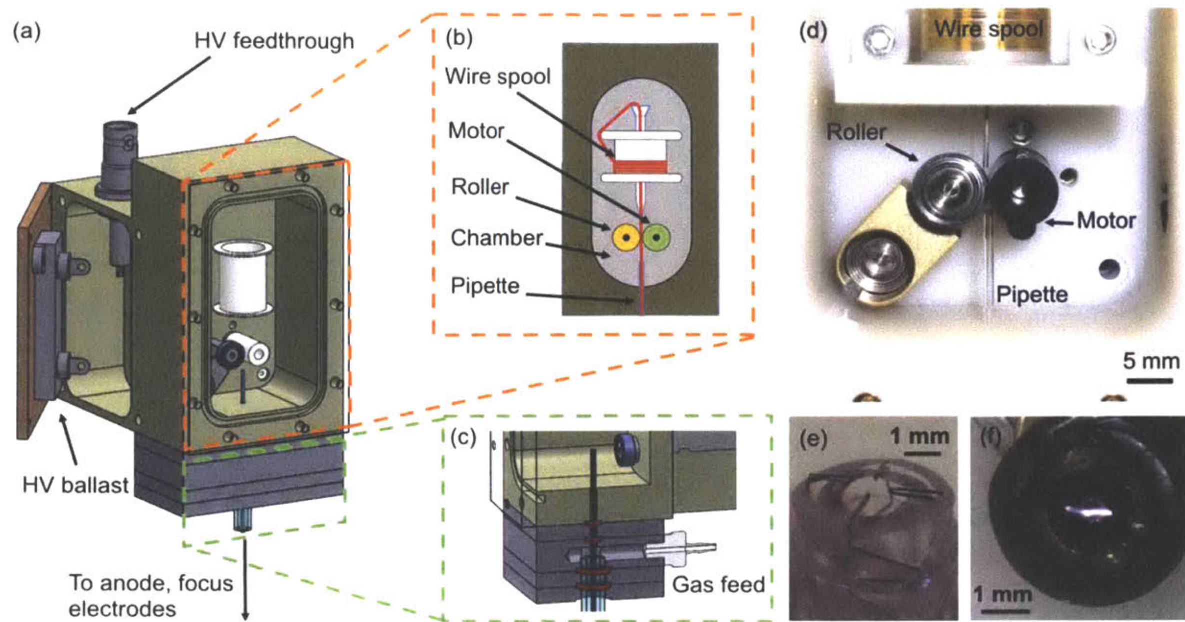

Figure 3. (a) CAD of printhead support system that supplies gas, electrical signals, and target wire to printhead; (b) CAD of target wire feed mechanism; (c) cross-section CAD showing the gas feed; (d) close-up photograph of implemented wire feed mechanism; (e) nozzle with electrode wires (f) plasma generated at nozzle tip. In (f), the longer anode electrode pair generates the plasma and compresses the beam, while the focus electrode pair, perpendicular to the anode pair, is used prevent pressure build-up. In this case, the plasma is formed between both anodes and the target wire; often, only one anode and the target are used.

and the target wire is shown in Fig. 3 (f).

The bias voltage applied to the anodes is regulated by a Keithley 2657A power supply. The power supply is a source-measuring unit that regulates the current, typically at a value between 0.5 and 1.5 mA. The resultant bias voltage, between 1 and 2.5 kV, flows through a 1 MΩ ballast resistor before reaching the anode electrodes; the ballast resistor prevents the parasitic capacitance of the circuit from rapidly charging and discharging, which would cause unwanted transient plasmas. The focus bias voltage is regulated by a HP 7516A power supply, which supplies a constant voltage (relative to ground) and no current; a 2 MΩ resistor between the power supply and ground minimizes the chance that an unwanted plasma connects the anode and focus

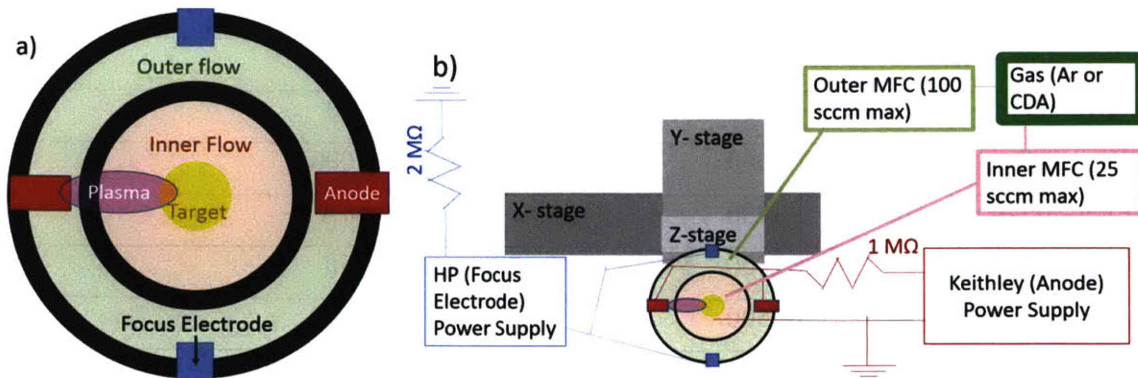

Figure 4. (a) Schematic of cross-section of printhead, and (b) overhead schematic of printhead with stages, gas flow, and electrical connections. In (a), the plasma forms between one of the anode electrodes and the target wire; due to the curvature of the spooled target wire, the target is rarely perfectly centered. Thus, the plasma will naturally form between the anode electrode that is closer to the target. The target wire is surrounded by inner and outer gas flows, each bounded by a thick tube wall. The anode electrodes push the deposit toward the center, while the focus electrodes draw it out. In (b), the printhead is mounted on the Z-stage, which is mounted on the Y-stage, which in turn is mounted on the X-stage. Two separate power supplies bias voltages to the anode and focus electrodes; both are referenced to ground. Two mass flow controllers meter gas from a common source (either a compressed-dry-air line or an argon tank) to the inner and outer flows. Neither diagram is to scale; the dimensions of the printhead are summarized in Table II.

electrodes, running through the HP power supply to the ground (Fig. 4 (b)). The dimensions of the printhead are summarized in Table II.

4.2- Gas Flow

Plasmas strike most easily in inert noble gases, in which there are few reactions to absorb energy from accelerated ions. Argon is a popular choice due to its inexpensiveness and large ionization cross-section. Heavy ions also increase the sputter yield, due to the increased mass and thus impulse incident on the sputter target [34]. For these reasons, many sputtering setups use argon. Because we do not work in an enclosure, if we want to use argon, we must ensure a steady flow of argon replenishes any gas that freely diffuses out to the atmosphere. However, our plasma

Measurement	Experimental Dimension (µm)	Simulation Dimension (µm)
Target Wire (diameter)	50	50
Inner Flow- ID of glass pipette	375	150
Inner Flow- OD of glass pipette	1000	1000
Outer Flow- ID of outer tube	3000	N/A
Anode-Target Gap	1500	750
Focus-Target Gap	2500	1400
Substrate-Target Gap	500-2500	200-3000

Table II: Summary of key dimensions of the printhead used in the experimental setup and the computational simualtions. The computational values were changed in the interest of computational stability and speed. The simulations do not have an outer gas flow; as such, there is no associated diameter.

is stable and easy to strike in air, and thus we do not need an argon atmosphere. Nevertheless, we incorporate the option to use an argon atmosphere. The majority of our results were obtained with compressed dry air; those results obtained in argon are noted as such explicitly.

Furthermore, a gas flow is essential to ensure that the sputtered material reaches the substrate. In traditional sputtering, the high vacuum ensures that the sputtered material flies directly from the sputtering target to the substrate; the mean free path is larger than (or at least, on the same order of magnitude as) the distance between the target and the substrate. However, in a microsputterer, where the aforementioned target-substrate distance is orders of magnitude greater than the mean free path, any sputtered atom must undergo what can be approximated as random walk, turning with every collision with the ambient gas. As in random walks, the fraction of atoms that reach the substrate scales as the square of the distance. By introducing a gas flow from the target to the substrate, we can direct the entire atmosphere, and thus the sputtered material, toward the substrate, minimizing the loss due to collisions. The random walk still occurs, but it is now relative to the gas flow.

A gas flow leading from the target to the substrate also assists in our focusing. The cathode fall, near the plasma, is very rich in ions, which we need to implement our focusing approach. A gas flow draws some ions out from the cathode fall, just as a plasma jet might extract ions from

near the electrodes to pattern a substrate [31].

These two purposes of the gas flow are best served by two different flows (Figs. 3 (c), 4(b)). An inner circular pipe with a small (0.44 mm^2) cross-section allows a relatively fast flow of gas to carry sputtered material at an initial speed of 20-100 cm/s toward the substrate. An outer annular pipe with a much larger cross-section (6.28 mm^2) floods the atmosphere surrounding the sputterer with 20-100 sccm at a velocity of 4-20 cm/s. The use of two flows allows to independently control the argon content of the atmosphere (when using argon) and the velocity of the gas flow. The two flows are controlled by two Unit MFC-1000 controllers; the inner flow's controller is rated for a maximum of 25 sccm, while the outer flow's controller is rated for 100 sccm. The controllers are independently adjusted using analog voltage inputs; when we sputter with air, we do not use the outer gas flow at all.

To characterize the focusing performance of this novel microsputterer, we (i) conducted simulations using COMSOL Multiphysics® (reported in Chapter 5), and (ii) tested the system experimentally (reported in Chapter 6); the results validate our proposed focusing method.

4.3- Wire Feed

While our work is still experimental, we recognize that a practical system needs to run for hours on end; during that time, the sputtering target will be depleted if is not somehow replenished. While the slow depletion of targets is not a major problem in traditional sputtering, the same depletion from a microsputtering target can change the behavior of a microsputterer, due to the greatly reduced length scale.

As a simple example, let us assume that a microsputterer is simply a $1:10^4$ model of an industrial sputterer. If a standard sputterer has an interelectrode distance of 1 m, the depletion of 1 kg off of a 2-inch diameter target only changes the distance by 2%. However, if we scale down the standard sputterer to a microsputterer with an interelectrode distance of 100 μm and a 5 μm diameter target wire, the depletion of 10 μg of gold (allowing for an equally-thick coating on an appropriately reduced area) multiplies the interelectrode distance by 26. Therefore, it is clear that depletion is a much more immediate need in microsputterers than in regular sputterers.

Target depletion is a pressing, common problem in microplasmas; many other reported

microplasma-based devices use clever geometries to prevent the sputtering of the cathode, while still allowing a plasma to form [24]. However, since sputtering is a goal of ours, we must instead accept depletion, while replenishing the depleted cathode as needed. In our design, target replenishing is done with a wire feed. We use a commercially-available 50 μm diameter gold wire for our target [47]. This wire is fed through a capstan-and-roller assembly (Fig. 3 (b)-(d)). A metal roller (that also serves as the electrical connection between the wire and the high-voltage power source) and a stepper motor (covered in a rubber sheath) hold the wire tightly between them. When the motorized stepper motor (FaulhaberAM1524, controlled by a Micromo MCST 3601 motion controller) is actuated, the wire is pushed through the assembly and down the inner gas sheath, a glass pipette. This lowers the tip of the wire, replenishing the depleted electrode (Fig. 3 (b), (d)). Currently, the controller is manually operated using both visual observation and a measurement of the microplasma's bias voltage to ensure a consistent geometry. In our experience, monitoring the anode voltage can ensure that the inter-electrode distance is constant to within 50 μm.

4.4- Substrate

To test the printhead, we printed on silicon wafers, sometimes coated with SiO_2 (to prevent a plasma from attaching itself to the substrate), and sometimes with both SiO_2 and a thin layer of chromium to act as an adhesion layer for the gold imprint (gold is known to not stick to many surfaces; chromium is an adhesion layer for gold commonly used in standard microfabrication). The distance between the printhead and the substrate is controlled by a Newport 433 ball bearing manual linear stage with an SM50 micrometer (50 mm of travel distance, 100 μm vernier resolution).

5- Simulation

5.1 - Model

Our four-electrode ion-drag focusing system is innovative, and as such, it was prudent to test the system computationally before committing to an experimental configuration. Simulation also produces results free of experimental error, allowing us to see trends that might otherwise not be statistically significant, due to large uncertainties in the experimental data.

Plasma simulation is a rich field, yielding many methods, models, and pieces of software. Atmospheric plasma simulation is a subfield of its own; much important work has been done recently [24],[48]-[51]. Most models rely on a fluid model, in which the fluid properties (i.e. pressure and velocity), plasma properties, (i.e., fraction of ions and electrons), and electromagnetic (EM) fields are tracked for each unit volume. Ionization and attachment equations, along with heat transfer and separate velocity calculations for ions and electrons further complicate the system. Kinetic theories, in which the velocity is expressed as a distribution, instead of a single value, for each unit volume, are more computationally intensive, but are necessary for plasmas driven by very-high-frequency electric fields. Fortunately, this is not the case in our setup.

However, even a simple fluid model becomes intractable once it is extended into the third dimension. Particularly, the dependencies between the physical quantities imply that all of the equations must be solved simultaneously –they are fully coupled. For example, the fluid velocity depends on and affects the Lorentz force, which depends on and affects the electric fields, which depends and affects on the charge distribution, which depends on the fluid velocity (and pressure). For a single unit volume, there are over a dozen equations, which then interact with the equations for each nearby (and far) unit volume. Nonlinear effects are common, and much of fusion research revolves around computing this model.

However, in the interests of putting together a framework that solvable in a reasonable time yet useful, we make several simplifications. Even though the volume charge and EM fields are interdependent, we neglect the effect of the volume charge on the EM field. We justify this by separating the volume into two spaces. In one space, the cathode fall, which is very near the target

wire, there is a relatively high positive space charge [28]. Elsewhere, however, the plasma has a relatively small space charge. For a qualitative analysis, we can thus ignore the effect of the space charge on the EM field everywhere far (> 50 μm) from the target wire.

Near the target wire, we implement the effect of the space charge by exploiting Debye shielding. In a highly ionized plasma, ions arrange themselves to shield the interior of the plasma from any electric fields. Although our plasma has a low degree of ionization (in a typical sputtering plasma, 0.1% of atoms are ionized), the high density causes a short Debye length, the characteristic distance over which electric effects are attenuated. Specifically, with the equation for a Debye length λ_D of

$$\lambda_D = \sqrt{\frac{\epsilon_0 k_b T}{n\, q^2}} = \sqrt{\frac{8.85\times10^{-12}\cdot1.38\times10^{-23}\cdot350}{1\times10^{-3}\cdot2.54\times10^{25}\cdot(1.5\times10^{-19})^2}}, \quad (4)$$

we estimate a Debye length of 8.65 nm, which is many orders of magnitude smaller than any of other dimension in the microplasma reactor. Thus, we approximate the area nearest the target wire as a floating potential; the high concentration of ions will enforce an equipotential across the entire cathode fall. The remainder of the plasma has a very small space charge, which does not affect the EM fields significantly [23].

However, this small space charge is still important for our ion-drag mechanism, as described earlier. We model this effect as a volume charge on each unit volume, proportional to the product of the electric field and the space charge. We do not account for recombination or ionization of the ions and neutrals; this is the most significant deviation from reality, although it is one that we must accept for computational feasibility. We justify this by claiming that the time-of-flight of the sputtered material is on the order of 1 ms, a time scale on which ionization effects are less significant.

Fluid conditions are somewhat simpler to model; we use the built-in COMSOL fluid model. For computational simplicity, we treat the fluid as incompressible. More detailed simulations suggest that the actual compression is very small; because of the very small length scales and high pressure involved, any small compression causes a large pressure gradient, and

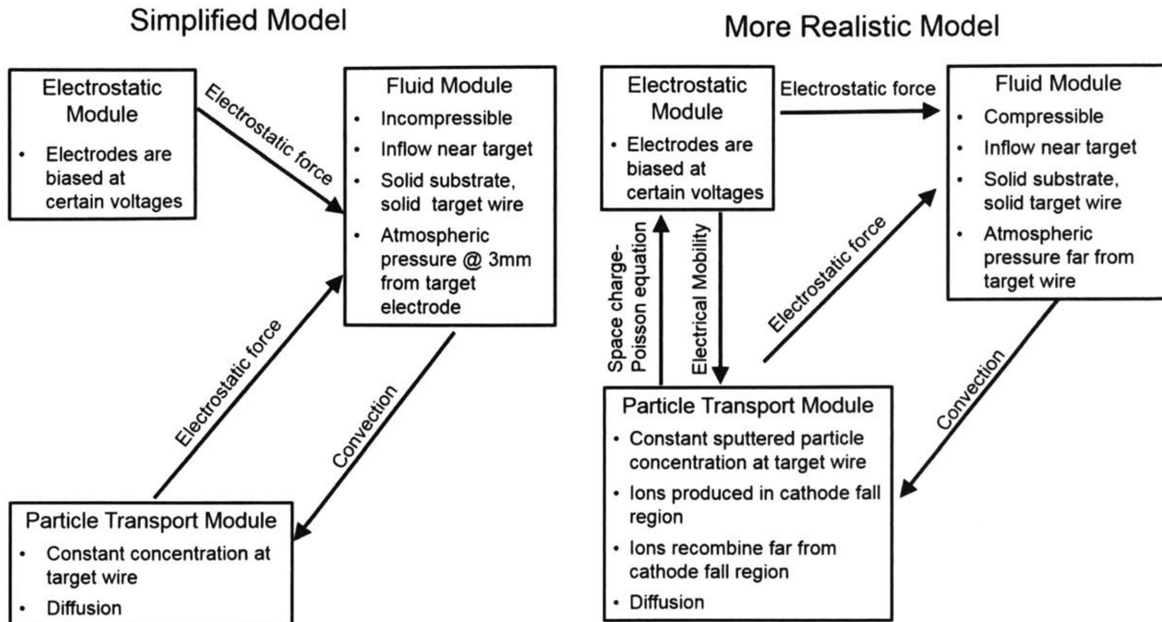

Figure 5. Schematic of the interaction of the three modules that compose the implemented simplified plasma model (left), and a more accurate plasma model for comparison (right). In the implemented model the electric field has no dependencies, greatly simplifying calculations; in reality, the electric fields depend on the charge density. In both models, the transport of ions and the movement of the gas are coupled.

thus an overwhelmingly large force. Because our simulation uses conditions with Reynolds numbers between 10 and 100, we also treat the flow as laminar. We neglect heat effects; experimental results show that there is no significant heating of either the electrodes or the atmosphere during normal operations.

Our quantity of interest is the sputter yield. We track this by introducing a concentration of solute at the target wire; the solute moves with convection and diffusion. For computational simplicity, we assume that the ion concentration is proportional to the sputter concentration; both are produced near the target wire and move identically through the fluid. Unfortunately, this requires that we neglect electric mobility, and, as already described, recombination, and ionization far from the target wire. A summary of the model, along with the major differences from a more realistic framework, can be seen in Fig. 5.

Boundary conditions and geometry follow reality closely (Fig. 6 and Table II).

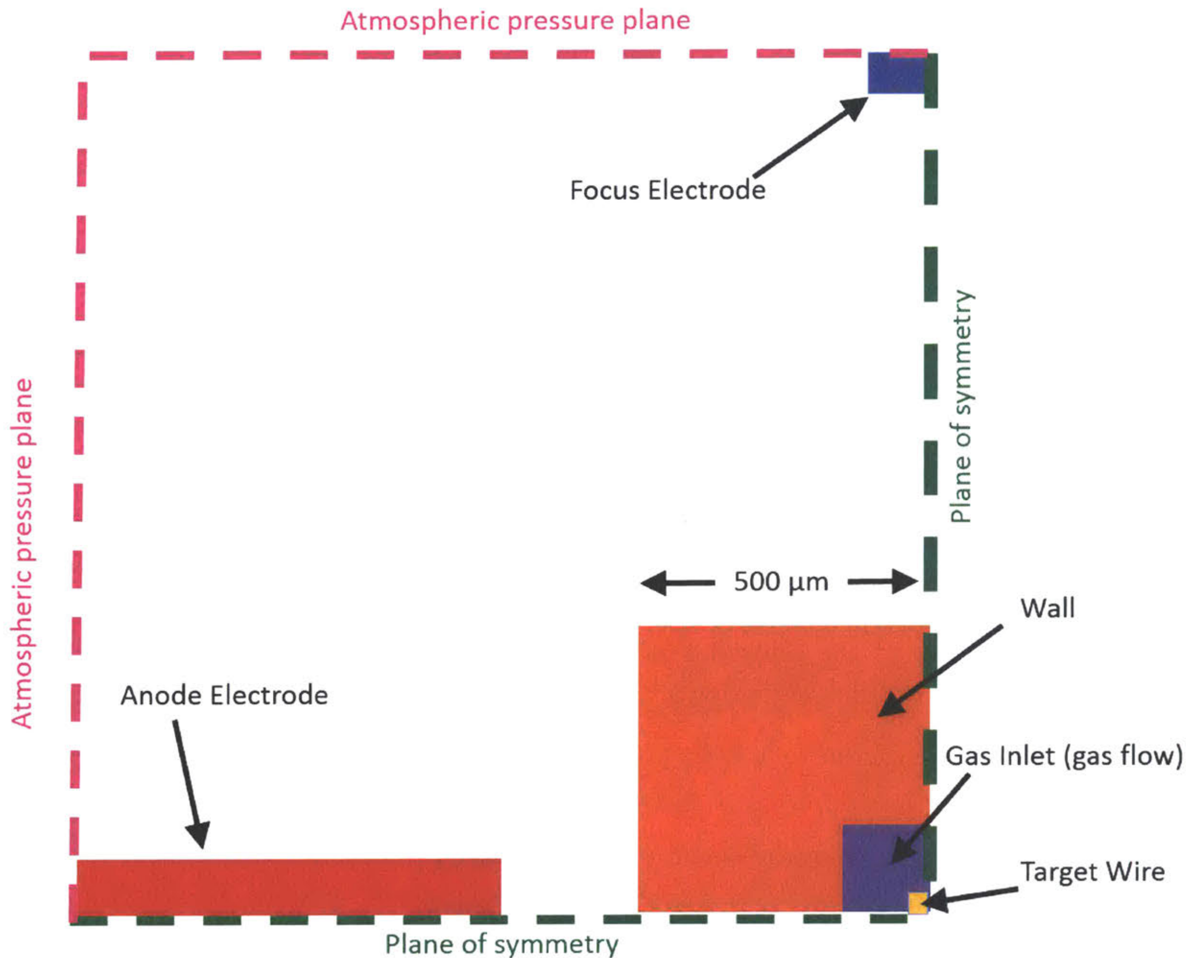

Figure 6. Top view of the geometry simulated, i.e., the upper left quadrant of the space between printhead tip and the substrate. The region is bounded by two planes of symmetry, the substrate, and two 3 mm-long walls at atmospheric pressure. Three electrodes (anode, focus, and target), biased at certain voltages, are placed at the top surface of the region of simulation. The substrate (not shown) is on the bottom of the simulated geometry. The geometry's values are based on our experimental setup, with slight deviations for computational stability. Additionally, the circular boundaries of reality are simulated as rectangles, to prevent difficulties with modeling circular geometries in rectangular finite-element meshes.)

Atmospheric pressure is enforced a large distance (3 mm) from the target wire. The volume flow rate in through each of the inlets is set explicitly. The electrodes are explicitly biased at certain

voltages, while the target wire is set as a floating potential. Distances mirror reality, although the inner gas flow is smaller in simulation than in reality for computational stability (see Table II). The outer gas flow is shown to have a negligible effect on the fluid motion; it is replaced by a boundary condition that simply enforced atmospheric pressure in the outer gas flow's inlet. This condition enhances the model's computational stability.

The computational stability of the model is of major concern. Because of the many interacting equations, the possibility exists for computational instabilities. The interactions present the possibility of positive feedback in errors, where, for example, a small, unphysical stream of ions far from the target wire can cause the simulation to assume that there is an electrostatic volume force that will draw more ions to the stream. In reality, such a stream would dissipate quickly, but COMSOL's search for a stationary solution can lead it down a wrong path. We mitigate this by carefully adjusting the coupling mechanism to try to stamp out nonphysical feedback effects quickly, with moderate success.

5.2- Results

In our model, we modify three parameters: the inner gas flow, focus voltage, and distance between the target wire and substrate. The anode voltage is set at the typical experimental value of 1 kV. We use the COMSOL optimization module to focus on a small region of the parameter space that allows for the desired focusing; we then explored the effects of modifying these parameters. In the simulations, we are attempting to optimize two values: the yield (fraction of sputtered material that reaches the substrate) and the line width (measured as full width half maximum, FWHM, i.e., the total width of the portion of the line that contains at least half the sputter concentration as the center). We use the COMSOL optimization module, with a Nelder-Mead algorithm, attempting to minimize a cost function *CF*

$$CF = \left(\frac{2 \cdot c_5}{c_{center}}\right)^6 + \left(\frac{0.01}{yield}\right)^6, \qquad (5)$$

where c_{center} is the total deposit on the line of symmetry (running from focus electrode to target wire, in the direction of the desired deposit), and c_5 is the total deposit on a line 5 μm away. The first fraction in the cost function thus will equal unity with a FWHM of 10 μm, and a greater value

(raised to the sixth power) for wider lines. The second term will equal unity with a yield of 1%, and a greater value (raised to the 6th power) for lower yields. The exponents insure that neither term of the cost function is too high; the cost function is an L_6 norm of our two constraints (in signal processing and other statistical studies, the L_6-norm is commonly used as a smoothed worst-case optimizer, i.e. an optimizer that attempts to ensure that the largest error in a fit is as small as possible, [52]). Repeated simulation runs showed that the "optimal" solution returned by the implemented model varied greatly based on the starting point of the optimization, suggesting that the cost function has several local minima. This makes both computational modeling and experimental exploration of the parameter space difficult. However, it means that even if the true "best" solution is hard to find, there are many solutions that offer some degree of success, in the form of an appreciable yield and reasonable focusing.

Selected results of the COMSOL modeling are shown in Figs. 7 to 10. For a suitable set of parameters, lines narrower than 20 μm (FWHM) are predicted, with a yield of 40%. Given that the implemented model is greatly simplified, no close match between the simulated absolute values and the experiments is expected; however, the model is valuable for establishing trends on how the different parameters influence the printed feature geometry.

The simulations showed that optimal narrow lines with appreciable yields have associated gas flows in which the velocity toward the substrate decreases slowly, in an approximately linear fashion, with minimal slowing down due to pressure differentials. If the gas flow is not large enough, convection is not able to carry the sputtered material to the substrate, diminishing the yield (Figs. 7 (b), 9 (b)). This is equivalent to a lens with a too-small focal length; perfect focus is achieved, but not at the substrate.

If the gas flow is too large, the gas travels at a very high velocity until it reaches the area of high pressure, resulting in insufficient residence time for the electrostatic forces to focus the gas flow before the hydrodynamic forces dominate and defocus the slightly-focused flow (Figs. 7 (c), 9 (c)). This is equivalent to a lens with a focal length that is too great –the gas impinges on the substrate before full focusing effects come to bear. This trend was confirmed by experiment.

The focus bias voltage also has an optimal value (Fig. 8). A larger magnitude of the focus bias voltage improves focusing by pulling the plasma toward the focus electrodes and thus

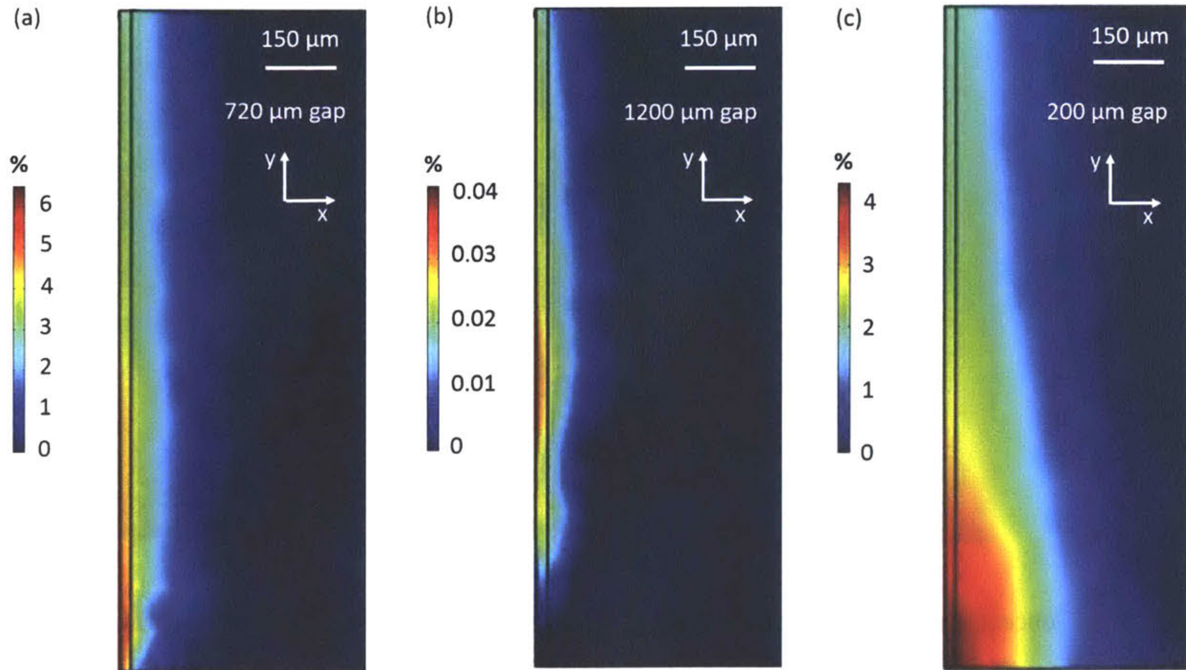

Figure 7. Concentration of sputtered material on the substrate for (a) optimally focused and (b), (c) non-optimally focused beams; concentration is normalized to the concentration at the target wire and is proportional to the thickness deposition rate at each point. Due to symmetry, only one quarter of the substrate is shown. Note the narrow width of the optimally focused and over-focused deposits ((a), (b)), as evidenced by the black vertical line 25 µm from the left edge on each plot that marks the boundary of the target wire. The x-direction runs between the anode electrodes, while the y-direction runs between the focus electrodes, and thus the direction of the printed line. In (a), we see an imprint significantly narrower than the target. While (b) also has a narrow imprint, the overly large gap decreases the yield unacceptably. Figure (c) shows a deposit, that, although asymmetric, is wider than the target. This is due to a decreased gap between the substrate and target, which causes a widening of the deposit due to a pressure buildup. These simulations were run with anode bias voltage equal to 1 kV, focus bias voltage equal to -750 V, and a gas flow rate of 33 sccm.

harnessing the hydrostatic pressure to decrease the line width; however, if the magnitude of the focus bias voltage is too large, the ions are drawn directly to the focus electrodes and never reach the substrate (Fig. 8 (b)). In practice, the optimal value of the focus bias voltage is highly dependent

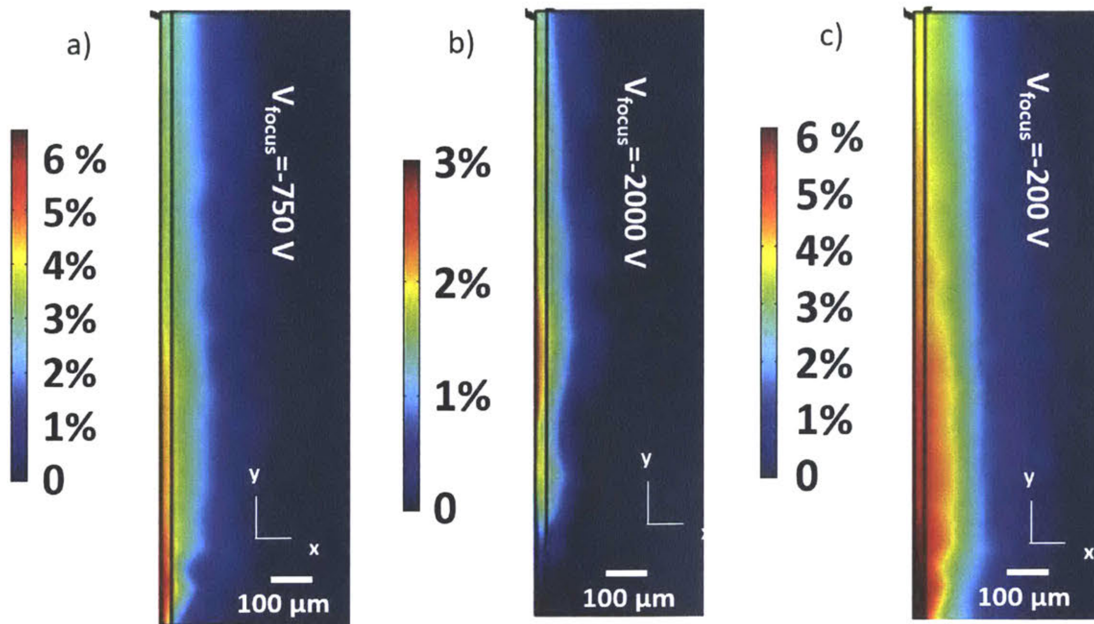

Figure 8. Concentration of sputtered material on the substrate for optimal (a) and non-optimal (b), (c) focus voltage. These graphs are analogous to those of Fig. 7, although are obtained by varying the focus voltage from the conditions that produced Fig. 7 (a). An ideal focus voltage produces Fig. 8 (a), in which the focus electrodes defocus the line enough to prevent a pressure buildup, allowing the deposition of a narrow line on the substrate. When the focus voltage's magnitude is too large (b), the defocusing prevents any pressure buildup, so the deposit is narrow, but much of the sputtered material is diverted to the focus electrodes instead of the substrate. Note that in (b), the deposit does not reach the portion of the substrate directly under the target wire; it is diverted in the y-direction towards the focus electrodes. If the focus voltage's magnitude is too small (c), the deposit is too wide, due to the pressure buildup described in Chapter 3.

on the gas flow, although the optimal focus bias voltage has the same order of magnitude as the anode bias voltage. In experiments, the focus voltage is also constrained by the possibility of a plasma forming between the anode and focus electrodes, bypassing the target wire. However, focus bias voltages of -700 V (i.e., 70% of the magnitude of the anode bias voltage) are still attainable.

Even though our simulation model is too crude to give us quantitative results, we still gain three important insights. First, the ideal parameters for focusing cause a smoothly slowing stream

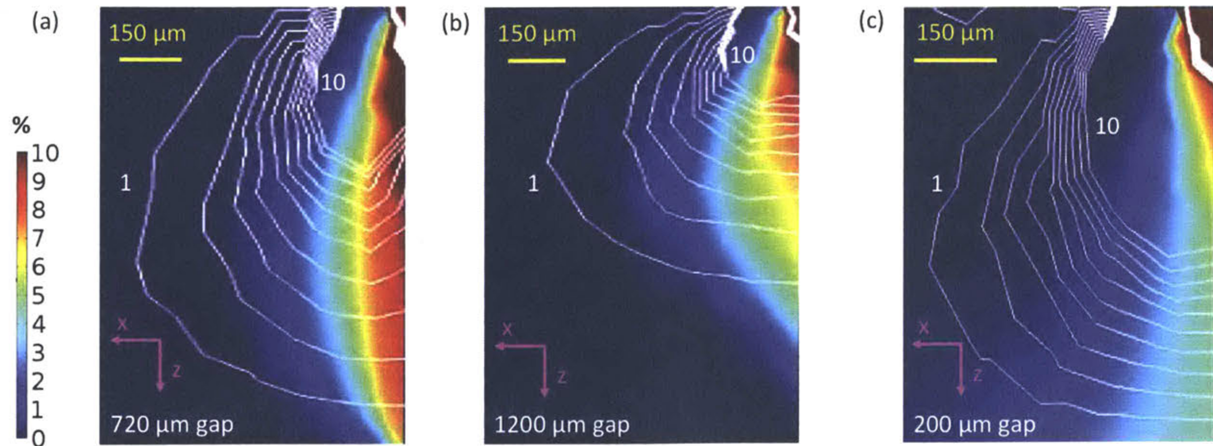

Figure 9. Side view of sputtered material concentration as the flow moves from target (top) to substrate (bottom). Optimally focused (a) and non-optimally focused (b), (c) beams are shown, with the same parameters used in Figure 7. As previously, the x-direction, in which the deposit is focused, runs between the anode electrodes, while the z-direction leads from the printhead to the substrate. To ease visualization, the color map is saturated at 10% of the material concentration at the target wire. White contour lines show the velocity of the gas flow toward the substrate, every 1 m/s from 1 to 10 m/s. A scale bar for the horizontal direction is provided, while the total vertical dimension (i.e., target-to-substrate gap) in each plot is 720 µm, 1200 µm, and 200 µm, respectively. Note that because of the varying gap, the scale is different in each dimension and each figure. With optimal focusing, the contour lines are spaced roughly evenly in the space directly below the target, and the sputtered material spreads slightly (due to diffusion) before it focuses on a spot (a projection of the line in the y-direction) downstream of the target. In (b), the sputtered material focuses on a spot above the substrate; because of the low gas flow rate near the substrate, most of the sputtered material does not reach the substrate. In (c), although some focusing is evident, the pressure forces a sharp defocusing. It can be seen from the spacing of the contour lines that the gas must decelerate quickly, slowing from 10 m/s to 0 m/s in approximately 100 µm.

toward the substrate; this can be accomplished by adjusting the substrate-target gap and the gas flow appropriately. Second, the focus voltage has an appropriate maximum –too high a voltage and the sputter deposit will never reach the substrate. Finally, we see the trade-off between focus and yield; as is evident from Fig. 10, we cannot simply optimize one and hope the other will follow –an appropriate yield will require some sacrifice in the deposit's width, and vice versa.

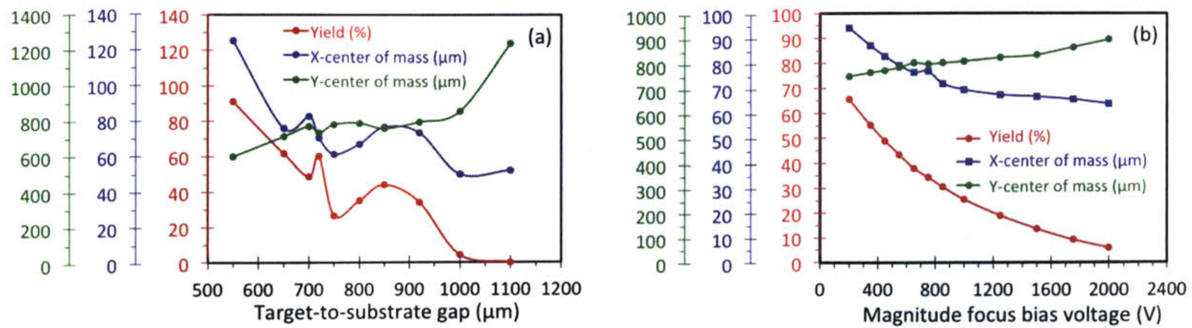

Figure 10. Yield and imprint center of mass in the x (anode-anode)- and y (focus-focus)-directions, vs. target-to-substrate gap (a) and magnitude of the (negative) focus bias voltage (b). As the substrate-to-target gap increases, less material reaches the substrate, although the beam's focus improves. Similarly, a larger magnitude of focus bias voltage compresses the beam better, but also draws the gas flow toward the focus electrodes and away from the substrate, decreasing yield. In (a), there are unexpected small variations near a gap of 700 µm, due to difficult-to-model interactions between the gas flow and the substrate near the point of optimal focusing. In (b), the center of mass in x decreases until the focus bias voltage is -750 V (signifying better focusing), but then begins to level off, suggesting that the optimal focus bias voltage for this set of parameters is -750 V; at that point, there is no longer a pressure differential which would defocus the line. At larger magnitudes, the focusing increases only marginally, as the flow's attraction toward the focus electrodes causes a vacuum, further improving focusing. This effect, however, is much less effective at focusing, and should be avoided to maximize yield. For each graph, the gas flow was held at 33 sccm; in (a) focus bias voltage = -750 V, in (b) substrate-to-target gap = 920 µm. The center of mass was measured for one quadrant of the imprint.

6-Experimental Results

6.1- Composition

EDX measurements were done with an EDAX energy dispersive X-Ray analysis tool. The data show that the imprint is nearly entirely made of gold, with traces of carbon contamination (Fig. 11). The silicon and oxygen peaks present are from the silicon-dioxide-coated silicon substrate used to collect the imprint. Notably, even though we sputter in atmosphere, no nitrogen is trapped in the deposit. Also notable is the absence of tungsten, indicating that the electrodes are not being sputtered, which is essential for long-term, reliable operation. This enables us to build future electrodes out of stainless steel, a material that is far easier to machine, but is less resistant to sputtering.

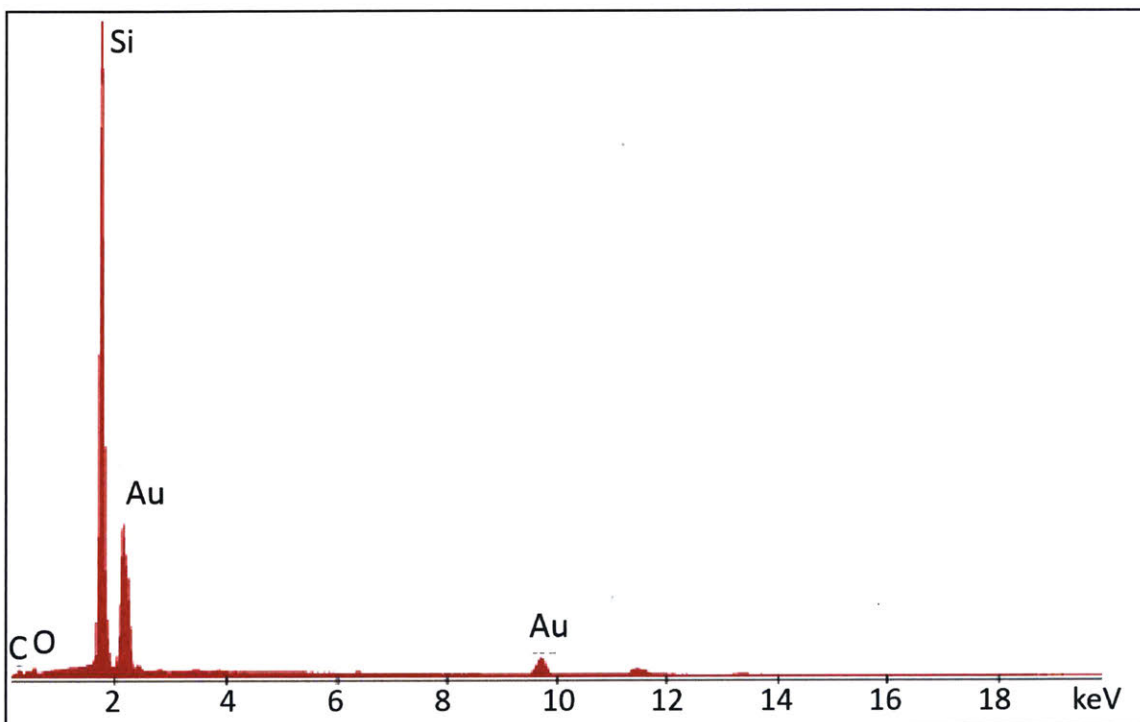

Figure 11. EDX measurements of a typical deposit, printed using our first-generation printer. Silicon, the substrate material, is dominant, while gold, the deposited material, is also present. Other than organic contaminants (carbon and oxygen), no other materials were detected. This suggests that the tungsten electrodes are not sputtered, allowing us to make future electrodes out of stainless steel, a material that is less resistant to sputtering but is easier to pattern.

6.2- Focusing

The ability to print a focused line made of sputtered material is the primary novelty of our work. While the width of the line is highly dependent on the parameters chosen, we present selected typical results. Specifically, in Fig. 12 we show a deposit without any focusing (i.e., with floating focus electrodes), one with mild focusing (the experimental analogy to Fig. 7 (c)), and a highly focused deposit (the experimental analogy to Fig. 7 (a)). We do not present experimental results that are a result of over-focused lines (e.g., an experimental result similar to what is shown to Fig. 7 (b)) because such a deposit is too thin to be accurately measured. In general, the experimental results match our computational predictions, with the exception of the focus voltage. The optimal focus voltage is much lower; its ideal magnitude is approximately 30-50%, rather than 100%, of the anode voltage.

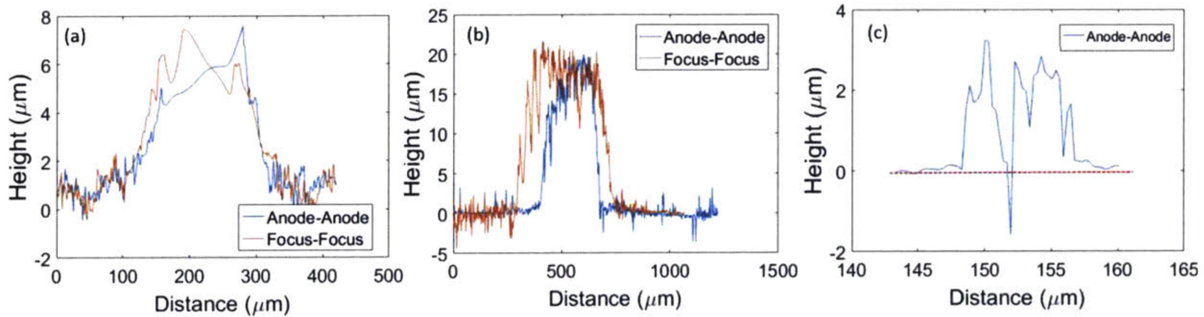

Figure 12. An unfocused (a), slightly focused (b), and highly focused (c) deposit; each deposit was created by running the printhead for 15 minutes. The unfocused deposit was produced without focus bias voltage (i.e., focus electrodes were left floating) and is roughly symmetrical. Significant asymmetry is apparent in the slightly focused deposit; the length of the imprint running from anode to anode is approximately 250 μm, while the length running from focus electrode to focus electrode is 410 μm. The highly focused deposit is 9 μm wide and approximately 3 μm thick; the deposit is cracked due to the stresses induced by the thickness of the deposit. The highly focused deposit is 3 mm long; it was produced without moving the substrate relative to the printhead. The apparent propagation of the crack in the SiO_2 film is an artifact of the confocal microscopy measurement technique. The length of the highly focused deposit (3 mm, focus-focus direction) cannot be clearly shown on the same scale its width is shown (9 μm, anode-anode direction). Note that (b) and (c) are the experimental analogs to Figs. 7(c) and (a), respectively; the absence of an analog to Fig. 7 (b) is discussed in the text.

The size of the deposit varies greatly. If the target wire is near the substrate (gap <1 mm), which minimizes collisions, the deposit is on the order of 200 μm in diameter (with possible deformation due to focusing), and approximately 1 μm in thickness for 900 seconds of operation. As the wire moves farther from the substrate, a halo forms around the deposit –a result of collisional scattering. Focusing helps limit this effect in the direction of focus, but the halo is still visible (Fig. 13). The halo is much thinner than the deposit, to the point of being non-continuous. However, is an undesirable artifact that can cause unwanted effects on sensitive electronics. Further plans to eliminate this halo, either with improved focusing or a shadow mask, are being pursued. Specifically, we note that the halo often forms under the opposite side of the positive column, i.e., toward the anode electrode that does not participate in the formation of the plasma. This suggests that the halo may be due to a low ion concentration near the target wire, on the side of the target wire that is farther from the plasma. Further plasma modeling and experimentation will help us understand this phenomenon and minimize the halo's presence.

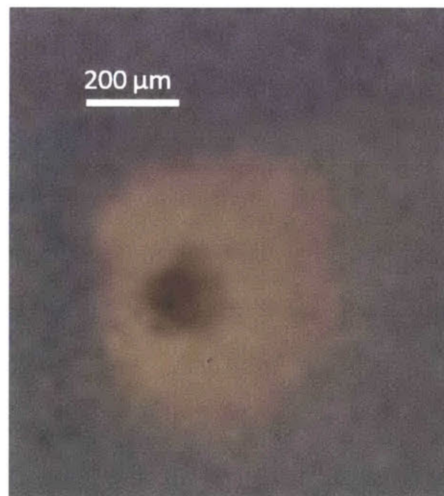

Figure 13. A deposit with a halo. Note the thick deposit in the center (dark gold), with a light gold halo surrounding it. The halo is more pronounced on the right side, which was not underneath the plasma. On the left side, the edge is much sharper; this asymmetry might help us understand the phenomenon and thus prevent the formation of the halo on either side. This deposit was obtained in an argon atmosphere (i.e., inner and outer argon flows).

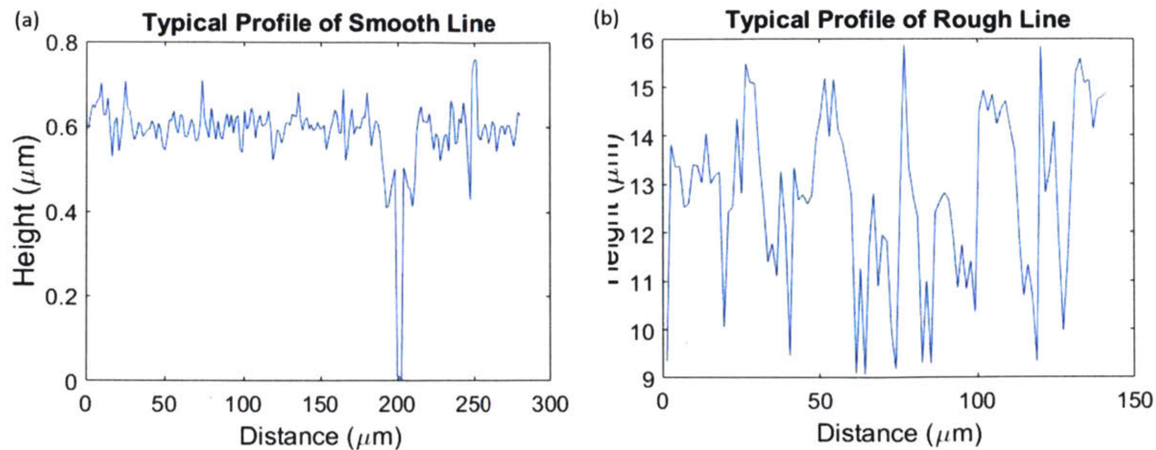

Figure 14. A one-dimensional scan of a smooth deposit (a), created by a well-behaved plasma, and a rough deposit (b), created by a varying plasma. The roughness ranges from 56 nm in the former case to 2.48 μm in the latter case. Note the small void in the left profile, exposing the underlying substrate and showing that the thickness of the deposit is approximately 10 times the roughness.

6.3- Roughness

Sputtering is known, in general, for producing smooth deposits. Microsputtering is no exception; if the plasma is stable and does not vary in its path between the electrodes or its voltage, the deposits are very smooth (Fig. 14 (a)). In these conditions, we estimate a roughness of 55 nm, with no apparent pattern to the peaks and valleys. This measurement was obtained by calculating the mean arithmetic deviation over a typical 20,000 μm^2 area. However, when the plasma varies in time, anchoring itself to different parts of the target wire, and/or varying wildly in voltage and interelectrode path, the deposit smoothness suffers (Fig. 14 (b)). Transient effects can lead to the deposition of a large amount of sputtered material in one spot, rather than a steady rain over an entire area.

6.4- Film microstructure

A major challenge in our printing was the microstructure of the deposits. Thornton's zone model, accepted since his seminal paper in 1977, has shown that the sputtered material, if it is buffeted about during its flight to the substrate, forms grain boundaries due to shadowing effects

[53]. If the pressure is low enough, the sputtered atoms fly directly to the substrate, impacting at a normal angle. However, at high pressure, the atoms that reach the substrate can be coming from any angle, and thus are likely to come across an already-deposited atom and stick to it. This causes grain boundaries (Fig. 15 (a)). If the substrate is heated to a temperature above 0.3 T_m, where T_m is the melting temperature of the sputtered material, thermal effects allow the just-deposited material to diffuse across the grain boundaries.

This model has stood for decades, and while there have been minor refinements [54],[55], it remains essentially accepted. Unfortunately, this model poses a problem for our material quality. Although heating the imprint is clearly a solution in many cases, we cannot use high temperatures at will to improve in general the microstructure of the film; for example, 0.3 T_m for gold is 128 °C, which is too hot for some plastic substrates. We cannot lower the pressure without changing our design drastically, and grain boundaries cause electrical conductivity to suffer. Burwell solved this problem with unintentional annealing; his apparatus raised the substrate temperature to 600 °C during deposition [37], well above 0.3 T_m for gold and therefore, more than enough to cause significant improvements in the microstructure of the deposit. While Abdul *et al.* do not report a deposition temperature [38],[39], their plasma used a heat-resistant conductive substrate as an anode and likely also heated it enough to anneal the deposit. We, in contrast separate the most energetic parts of our plasma from our substrate; as a matter of fact, tests with LDPE show that our substrate does not reach 100 °C; it might be possible to use infrared light or a heated bed to moderately increase the temperature of the imprints and achieve inter-grain diffusion, albeit not to the degree described in Thornton's zone model. This is something that should be explored in future work.

We instead glean an insight from HiPIMS, or High-Power Impulse Magnetron Sputtering. In HiPIMS, very high current density on a sputtering target ionizes a large fraction (>10%) of the sputtered material. This is caused by a high concentration of sputtered material in the plasma; the sputtered material causes a pressure that prevents gas from entering the plasma. As a result, the sputtered material becomes the dominant species in the plasma, hence becoming highly ionized. While such a high current would normally melt the sputtering target, if it is only applied in short bursts (impulses), it does not. By applying a negative voltage to the substrate, researchers have

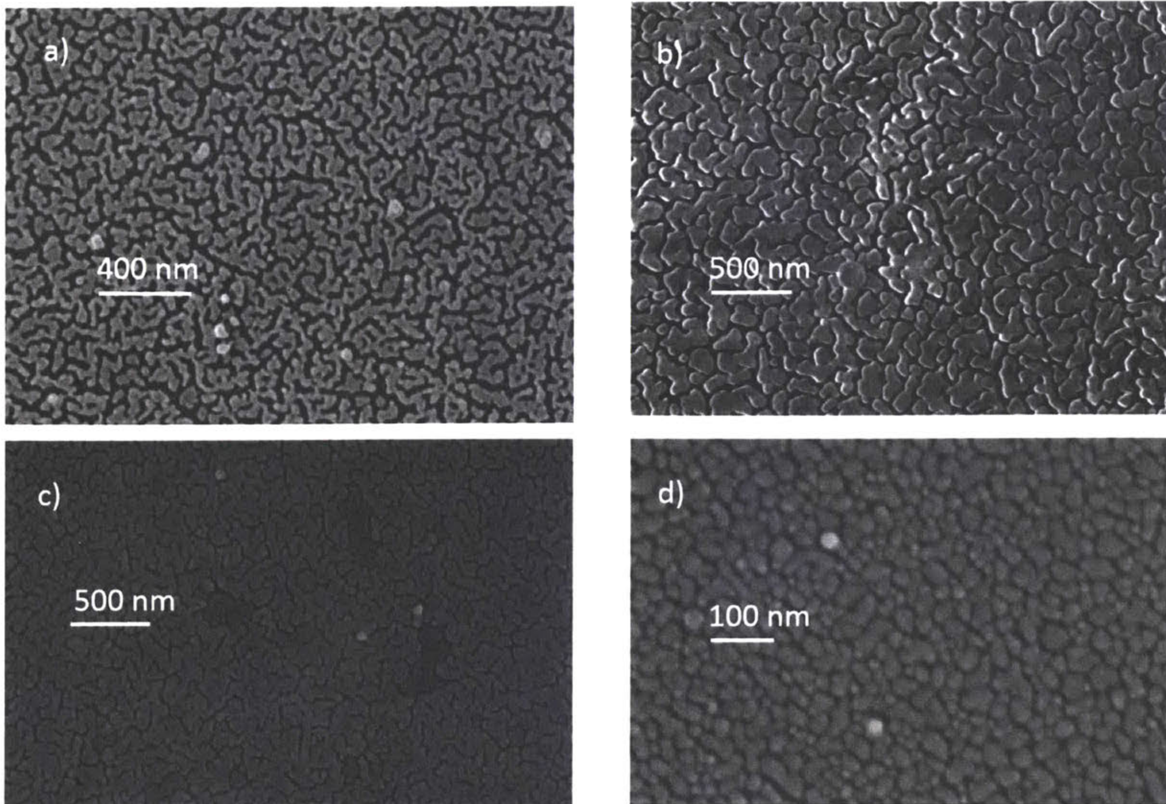

Figure 15. SEM micrographs of deposits microsputtered under varying conditions. With a small (5 sccm) inner gas flow and floating bias voltage on the substrate (a), the deposits are porous and have a meandering grain structure (a). When the gas flow increases to 25 sccm (b), the spaces between the grains are much smaller, although the grain structure still dominates. Once the substrate is biased (c), the grains merge into a single, continuous deposit. Sample charging causes the electrically isolated spots in (c) to appear darker, confirming that the majority of the deposit is electrically conductive. However, if the substrate is negatively biased (d), nanoparticles appear, instead of a meandering grain structure. These deposits were obtained in an argon atmosphere.

been able to attract the ionized sputtered material toward the substrate; they impact the substrate at a high speed, resulting in superior adhesion and material quality.

Our microsputterer is not pulsed, nor does it use magnetic fields. It is, however, high-intensity; the current densities of our setup (500 kA/m^2) are even greater with those of HiPIMS [56],[57]. However, we do not ionize the sputtered material in the same way that HiPIMS does; because our target is so small, the sputtered material cannot push out the surrounding gas.

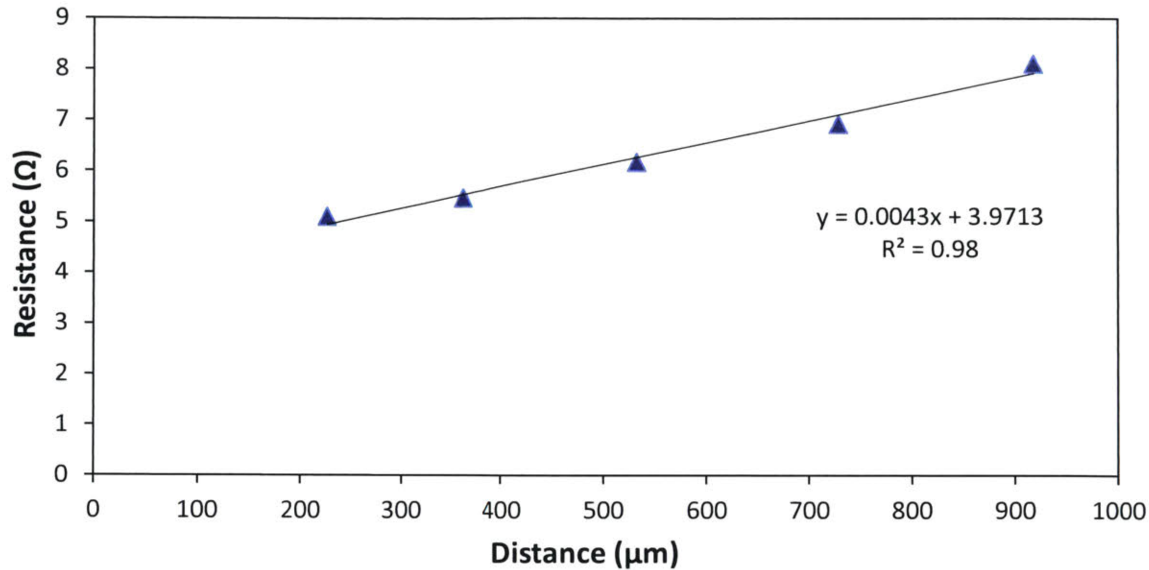

Figure 16. Electrical resistance measurements of a deposit. Probes were placed with a variety of spacings in a conductive sample, resulting in a resistivity of 4.3 Ω/mm. The sample had a cross-sectional area of 261 μm^2, yielding a total resistivity of 1.1 μΩ·m.

However, even if we do not ionize the sputtered material in the same way that HiPIMS does, we can use ion-drag focusing to attract the ionized argon atoms to the substrate, and the argon will drag the sputtered gold with it. While we may not get the same adhesion as HiPIMS, we will avoid the problems associated with Thornton's model. To show that our method will work with non-conductive substrates, we bias a metal plate under the substrate, rather than the substrate itself.

The experimental results to control the grain microstructure are promising. An early test involved using the inner sheath's gas flow to minimize grain boundaries; results are shown in Fig. 15 (a) and (b). Later tests involving biasing the substrate, or a piece of metal 1 mm beneath the substrate show two regimes of interest. In one case, when the metal beneath the substrate is grounded, very dense, continuous structures form (Fig. 15 (c)); grain boundaries are present, but subtler, and the majority of the deposit is electrically continuous. In the other case, when the substrate itself is grounded, or when the metal beneath it is negatively biased, small, distinct nanoparticles (approximately 50 nm in size) form (Fig. 15 (d)). These represent aggregated gold

sputter that is drawn toward the substrate with great force, eventually impacting. However, the substrate's voltage affects the sputtering mechanism, preventing continuous films from developing. This process is not yet well understood, but it might be a method to cheaply produce nanoparticles of a desired size.

Although SEM micrographs suggest that our deposits are continuous, it is difficult to accurately measure the conductivity of the samples; due to gold's poor adhesion to substrates, probes tend to damage the deposit. In the presence of gas flow without electrostatic assistance, resistance was measured at ~65X bulk resistance (Fig. 16).

6.5- Deposition Rates

The deposition rate varies greatly based on the operational parameters, e.g., bias voltages, flow rates, substrate-to-printhead separation. Specifically, anode bias voltages below 300 V tend to yield very thin depositions, or no depositions at all, with the yield increasing as the voltage does until approximately 700 V. If the voltage is too low, the ions cannot sputter enough material to create measurable deposits.

As we would expect from the simulation results, the deposition rate also varies greatly based on the target-to-substrate gap and the inner sheath gas flow. When the gap is too large or the flow is too slow, very little material is deposited; if conditions are right, the deposits are thicker. Under conditions of ideal focusing (Fig. 12 (c)), we estimate a volume deposition rate of 200 $\mu m^3/s$, which is comparable with other reports on microplasma printing when similar currents are used [37],[38]. Higher flows and smaller gaps lead to deposition rates 10 times greater.

7- Future Work

In this thesis, we provided a proof-of-concept demonstration of an ion-drag focused microsputterer; this preliminary exploration can be expanded in a number of directions that can be grouped into three categories: material, resolution, and control.

First of all, the deposited material must be improved. While we have made significant progress in the optimization of the microstructure of the material, we still need to demonstrate electrical conductivities close to those of the bulk metal; it is possible that a mild annealing of the imprint will result in a significantly better electrical conductivity. The material must also be made to adhere to a substrate; early experiments with rougher substrates (such as paper) are promising. Adhesion layers are also currently studied.

MEMS and microelectronics require more than metals. Even the creation of interconnects requires dielectric layers to electrically insulate stacks of conductive layers that run at different depths; the deposition of functional materials, e.g., piezoresistive or semiconducting, is also required in many transducers. Toward that end, we must expand our material set. While sputtering in large-scale reactors is readily conducted on many materials, we must demonstrate microsputtering of a number of materials of interest, preferably with a single apparatus to avoid problems with alignment and sample contamination between prints. This might be accomplished with an innovative multi-wire feed, currently in development.

While regular sputterers can easily sputter insulators by coating a conductive target with an insulator, forming a plasma between the conductive target and another electrode, and letting the plasma sputter off the insulation coating (taking care to avoid charge buildup by using RF plasmas), we cannot coat a continuously-fed wire. Thus, we will need to develop another method to deposit insulators. We are considering depositing compounds that start as a sputtered beam from conductive sources that reacts to become non-conductive *in situ*.

While we have demonstrated focusing, we still must eliminate the thin halo surrounding our deposits, and in general, improve the minimum feature size to ~1 μm. Work has begun with shadow masks, both those attached to the substrate and those attached to the printhead. Better plasma modeling will also improve focusing, and perhaps the exploration of other means of confinement, e.g., magnetic.

Viable AM techniques require consistency. Our methods must be fine-tuned to minimize variance, allowing us to achieve optimal results every time. Feedback control is essential for this.

Finally, we must also ensure that the geometry of the imprint is consistent. Our second-generation printhead has already improved in this area; the electrodes are rigid, and thus no longer shift slightly. This has improved repeatability; with identical parameters, we can achieve identical results. More work remains though, to make reliable additive manufacturing via microsputtering a reality.

8-Bibliography

[1] Conner, B. P., Manogharan, G. P., Martof, A. N., Rodomsky, L. M., Rodomsky, C. M., Jordan, D. C., & Limperos, J. W. (2014). Making sense of 3-D printing: creating a map of additive manufacturing products and services. *Additive Manufacturing*, *1–4*, 64–76.

[2] Herzog, D., Seyda, V., Wycisk, E., & Emmelmann, C. (2016). Additive manufacturing of metals. *Acta Materialia*, 117, 371-392.

[3] Olvera-Trejo, D., & Velásquez-García, L. F. (2016). Additively manufactured MEMS multiplexed coaxial electrospray sources for high-throughput, uniform generation of core–shell microparticles. *Lab on a Chip*, *16*(21), 4121–4132.

[4] Skylar-Scott, M. A., Gunasekaran, S., & Lewis, J. A. (2016). Laser-assisted direct ink writing of planar and 3D metal architectures," *Proc. Nat. Acad. Sci. USA* 113 (22) 6137–42.

[5] MacDonald, E., & Wicker, R. (2016). Multiprocess 3d printing for increasing component functionality. *Science*, *353*(6307), aaf2093.

[6] Hirt, L., Reiser, A., Spolenak, R., & Zambelli, T. (2017). Additive manufacturing of metal structures at the micrometer scale. *Advanced Materials*, *29*(17), 1604211.

[7] Li, Q., & Lewis, J. A. (2003). Nanoparticle inks for directed assembly of three-dimensional periodic structures. *Advanced Materials*, *15*(19), 1639–1643.

[8] Ahn, B. Y. *et al.* (2009). Omnidirectional printing of flexible, stretchable, and spanning silver microelectrodes. *Science* 323(5921), 1590-1593.

[9] Walker, S. B., & Lewis, J. A. (2012). Reactive silver inks for patterning high-conductivity features at mild temperatures. *Journal of the American Chemical Society*, *134*(3), 1419–1421.

[10] Schneider, J., *et al.* (2016). Electrohydrodynamic NanoDrip printing of high aspect ratio metal grid transparent electrodes. *Advanced Functional Materials*, *26*(6), 833–840.

[11] Visser, C. W. *et al.* (2015). Toward 3D printing of pure metals by laser-induced forward transfer. *Adv. Mater.*, 27: 4087–4092.

[12] van Oven, J. C., Berwald, F., Berggren, K. K., Kruit, P., & Hagen, C. W. (2011). Electron-beam-induced deposition of 3-nm-half-pitch patterns on bulk Si. *Journal of Vacuum Science*

& Technology B, Nanotechnology and Microelectronics: Materials, Processing, Measurement, and Phenomena, *29*(6), 06F305.

[13] Botman, A., Hesselberth, M., & Mulders, J. J. L. (2008). Improving the conductivity of platinum-containing nano-structures created by electron-beam-induced deposition. *Microelectronic Engineering*, *85*(5), 1139–1142.

[14] Roberts, N., D. Fowlkes, J., A. Magel, G., & D. Rack, P. (2013). Enhanced material purity and resolution via synchronized laser assisted electron beam induced deposition of platinum. *Nanoscale*, *5*(1), 408–415.

[15] Takai, T., Nakao, H., & Iwata, F. (2014). Three-dimensional microfabrication using local electrophoresis deposition and a laser trapping technique. *Optics Express*, *22*(23), 28109–28117.

[16] Espalin, D., Muse, D.W., MacDonald, E., Wicker R. B. (2014). 3D printing multi-functionality: structures with electronics. *Int. J. Adv. Manuf. Technol.* 72, 963–978.

[17] Sun, Z. & Velásquez-García, L. F. (2017) Monolithic FFF printed, biodegradable, biocompatible, dielectric–conductive microsystems," *Journal of Microelectromechanical Systems, 26*(6), 1356 – 1370.

[18] Mireles, J., *et al.* (2013). Development of a fused deposition modeling system for low melting temperature metal alloys. *Journal of Electronic Packaging*, *135*(1), 011008.

[19] Swensen, J. P., Odhner, L. U., Araki, B., & Dollar, A. M. (2015) Printing three-dimensional electrical traces in additive manufactured parts for injection of low melting temperature metals. *J. Mech. Robotics* 7, 21004.

[20] Suryavanshi, A. P., & Yu, M.-F. (2006). Probe-based electrochemical fabrication of freestanding Cu nanowire array. *Applied Physics Letters*, 88(8), 083103.

[21] Hirt, L. *et al.* (2016). Template-free 3D microprinting of metals using a force-controlled nanopipette for layer-by-layer electrodeposition. *Advanced Materials*, *28*(12), 2311–2315.

[22] Suryavanshi, A. P., & Yu, M.-F. (2007). Electrochemical fountain pen nanofabrication of vertically grown platinum nanowires. *Nanotechnology*, *18*(10), 105305.

[23] Llewellyn-Jones, F. (1966). *The glow discharge.* London: Methuen.

[24] Papadakis A P, Rossides S., & Metaxas A. C. (2011). Microplasmas: a review, *The Open Applied Physics Journal 4*(1) 45–63.

[25] Loeb, L. B. (1939). *Fundamental Processes in Electrical Discharges in Gases*, New York: Wiley.

[26] Paschen, F. (1889). Ueber die zum funkenübergang in luft, wasserstoff und kohlensäure bei verschiedenen drucken erforderliche potentialdifferenz. *Annalen Der Physik*, *273*(5), 69–96.

[27] Foest, R., Schmidt, M., & Becker, K. (2006). Microplasmas, an emerging field of low-temperature plasma science and technology. *International Journal of Mass Spectrometry*, *248*(3), 87–102.

[28] Chapman, B. (1980). *Glow discharge processes: Sputtering and plasma etching*. New York, NY: Wiley.

[29] Eijkel, J. C. T., Stoeri, H., & Manz, A. (1999). A molecular emission detector on a chip employing a direct current microplasma. *Analytical Chemistry*, *71*(14), 2600–2606.

[30] Schoenbach, K. H. (2013). High-pressure microcavity discharges In P. K. Chu, X. Lu (Eds.), *Low temperature plasma technology: Methods and applications* (pp. 97-118). Boca Raton, FL: CRC Press.

[31] Aragão, E. C. B. B. *et al.* (2014). Low temperature microplasma jet at atmospheric pressure for inducing surface modification on polyethylene substrates. *American Journal of Condensed Matter Physics*, *4*(3A), 1–7.

[32] Zhu, W. *et al.* (2007). Direct current planar excimer source. *Journal of Physics D: Applied Physics*, *40*(13), 3896.

[33] Richmonds, C., & Sankaran, R. M. (2008). Plasma-liquid electrochemistry: Rapid synthesis of colloidal metal nanoparticles by microplasma reduction of aqueous cations. *Applied Physics Letters*, *93*(13), 131501.

[34] Yamamura, Y., Matsunami, N., & Itoh, N. (1982). A new empirical formula for the sputtering yield. *Radiation Effects*, *68*(3), 83–87.

[35] Oliva-Florio, A., Baragiola, R. A., Jakas, M. M., Alonso, E. V., & Ferrón, J. (1987). Noble-gas ion sputtering yield of gold and copper: Dependence on the energy and angle of incidence of the projectiles. *Physical Review B*, *35*(5), 2198–2204.

[36] Wasa, K., & Hayakawa, S. (1992). *Handbook of sputter deposition technology.* Westwood, NJ: Noyes.

[37] Burwell, E. (2016). *A microplasma-based sputtering system for direct-write, microscale fabrication of thin-film metal structures* (MS Thesis, Case Western Reserve University, Accession No. 1449545772).

[38] Abdul-Wahed, A. M., Roy, A. L., Xiao, Z., & Takahata, K. (2016). Direct writing of thin and thick metal films via micro glow plasma scanning. In *2016 IEEE 29th International Conference on Micro Electro Mechanical Systems (MEMS)* (pp. 443–446).

[39] Abdul-Wahed, A. M., Roy, A. L., & Takahata, K. (2016a). Microplasma drawing of thermocouple sensors. In *2016 IEEE SENSORS* (pp. 1–3).

[40] Schumacher, U. (2001). Status and problems of fusion reactor development. *Naturwissenschaften*, *88*(3), 102–112.

[41] Foster, J. S., Lawrence, E. O., & Lofgren, E. J. (1953). A high vacuum high speed ion pump. *Review of Scientific Instruments*, *24*(5), 388–390.

[42] Hall, L. D. (1958). Electronic ultra-high vacuum pump *Review of Scientific Instruments*, *29*(5), 367-370.

[43] Grzebyk, T., Knapkiewicz, P., Szyszka, P., Górecka-Drzazga, A., & Dziuban, J. A. (2016) MEMS ion-sorption high vacuum pump. *Journal of Physics: Conference Series 773*(1), 012047.

[44] Carleton, F. B. & Weinberg, F. J. (1987). Electric field-induced flame convection in the absence of gravity, *Nature 330*(6149), 635.

[45] Papac, M. J. & Dunn-Rankin, D. (2008). Modelling electric field driven convection in small combustion plasmas and surrounding gases, *Combustion Theory and Modelling 12*(1), 23-44.

[46] Sefta, F., Juslin, N., Hammond, K.D., & Wirth, B.D. (2013). Molecular dynamics simulations on the effect of sub-surface helium bubbles on the sputtering yield of tungsten. *Journal of Nuclear Materials*, *438*, S493-S496.

[47] http://www.sigmaaldrich.com/catalog/product/aldrich/gf34620016?lang=en®ion=US

[48] Farouk, T. *et al.* (2007). Modeling of direct current micro-plasma discharges in atmospheric pressure hydrogen. *Plasma Sources Sci. Technol. 16,* 619.

[49] Hong, Y. J., Lee, S. M., Kim, G. C., & Lee J K. (2008). Modeling high-pressure microplasmas: comparison of fluid modeling and particle-in-cell Monte Carlo collision modeling. *Plasma Processes Polym. 5*, 583–592.

[50] Wilson, C. G., Gianchandani, Y. B., Arslanbekov, R. R., Kolobov, V., & Wendt, A. E. (2003). Profiling and modeling of DC nitrogen microplasmas. *Journal of Applied Physics*, *94*(5), 2845–2851.

[51] Becker, K. H., Schoenbach, K. H., & Eden, J. G. (2006). Microplasmas and applications. *Journal of Physics D: Applied Physics*, *39*(3), R55.

[52] Cheng, Q. S., Bandler, J. W., & Koziel, S. (2015). A review of implicit space mapping optimization and modeling techniques. In *Numerical Electromagnetic and Multiphysics Modeling and Optimization (NEMO), 2015 IEEE MTT-S International Conference on* (1-3).

[53] Thornton, J. A. (1977). High rate thick film growth. *Annual Review of Materials Science*, *7*(1), 239–260.

[54] Messier, R., Giri, A. P., & Roy, R. A. (1984). Revised structure zone model for thin film physical structure. *Journal of Vacuum Science & Technology A: Vacuum, Surfaces, and Films*, *2*(2), 500–503.

[55] Kluth, O., Schöpe, G., Hüpkes, J., Agashe, C., Müller, J., & Rech, B. (2003). Modified Thornton model for magnetron sputtered zinc oxide: film structure and etching behaviour. *Thin Solid Films*, *442*(1), 80–85.

[56] Brenning, N., Axnäs, I., Raadu, M. A., Lundin, D., & Helmerson, U. (2008). A bulk plasma model for DC and HiPIMS magnetrons. *Plasma Sources Science and Technology*, *17*(4), 045009.

[57] Anders, A. (2014). A review comparing cathodic arcs and high power impulse magnetron sputtering (HiPIMS). *Surface and Coatings Technology*, *257*, 308–325.